PHYSICAL REVIEW C **89**, 015502 (2014)

Improved measurement of the $2\nu\beta\beta$ half-life of ^{136}Xe with the EXO-200 detector

J. B. Albert,[1] M. Auger,[2] D. J. Auty,[3] P. S. Barbeau,[4] E. Beauchamp,[5] D. Beck,[6] V. Belov,[7] C. Benitez-Medina,[8] J. Bonatt,[9,4] M. Breidenbach,[10] T. Brunner,[4] A. Burenkov,[7] G. F. Cao,[11] C. Chambers,[8] J. Chaves,[4] B. Cleveland,[5,*] S. Cook,[8] A. Craycraft,[8] T. Daniels,[9] M. Danilov,[7] S. J. Daugherty,[1] C. G. Davis,[12] J. Davis,[4] R. DeVoe,[4] S. Delaquis,[2] A. Dobi,[12] A. Dolgolenko,[7] M. J. Dolinski,[13] M. Dunford,[14] W. Fairbank Jr.,[8] J. Farine,[5] W. Feldmeier,[15] P. Fierlinger,[15] D. Franco,[2] D. Fudenberg,[4] G. Giroux,[2] R. Gornea,[2] K. Graham,[14] G. Gratta,[4] C. Hall,[12] K. Hall,[8] C. Hargrove,[14] S. Herrin,[10] M. Hughes,[3] X. S. Jiang,[11] A. Johnson,[10] T. N. Johnson,[1] S. Johnston,[9] A. Karelin,[7] L. J. Kaufman,[1] R. Killick,[14] S. Kravitz,[4] A. Kuchenkov,[7] K. S. Kumar,[9] D. S. Leonard,[16] F. Leonard,[14] C. Licciardi,[14] R. MacLellan,[10] M. G. Marino,[15,†] B. Mong,[5] M. Montero Díez,[4] D. Moore,[4] R. Nelson,[17] K. O'Sullivan,[4,‡] A. Odian,[10] I. Ostrovskiy,[4] C. Ouellet,[14] A. Piepke,[3] A. Pocar,[9] C. Y. Prescott,[10] A. Rivas,[4] P. C. Rowson,[10] M. P. Rozo,[14] J. J. Russell,[10] A. Sabourov,[4,§] D. Sinclair,[14,¶] K. Skarpaas,[10] S. Slutsky,[12] V. Stekhanov,[7] V. Strickland,[14,¶] M. Tarka,[6] T. Tolba,[2] D. Tosi,[4] K. Twelker,[4] P. Vogel,[18] J.-L. Vuilleumier,[2] A. Waite,[10] J. Walton,[6] T. Walton,[8] M. Weber,[2] L. J. Wen,[4] U. Wichoski,[5] J. Wodin,[10,‖] J. D. Wright,[9] L. Yang,[6] Y.-R. Yen,[12] O. Ya. Zeldovich,[7] and Y. B. Zhao[11]

(EXO Collaboration)

[1]*Physics Department and CEEM, Indiana University, Bloomington, Indiana 47405, USA*
[2]*LHEP, Albert Einstein Center, University of Bern, Bern, Switzerland*
[3]*Department of Physics and Astronomy, University of Alabama, Tuscaloosa, Alabama 35487, USA*
[4]*Physics Department, Stanford University, Stanford, California 94305, USA*
[5]*Department of Physics, Laurentian University, Sudbury, Ontario, Canada*
[6]*Physics Department, University of Illinois, Urbana-Champaign, Illinois 61801, USA*
[7]*Institute for Theoretical and Experimental Physics, Moscow, Russia*
[8]*Physics Department, Colorado State University, Fort Collins, Colorado 80523, USA*
[9]*Physics Department, University of Massachusetts, Amherst, Massachusetts 01003, USA*
[10]*SLAC National Accelerator Laboratory, Menlo Park, California 94025, USA*
[11]*Institute of High Energy Physics, Beijing, China*
[12]*Physics Department, University of Maryland, College Park, Maryland 20742, USA*
[13]*Department of Physics, Drexel University, Philadelphia, Pennsylvania 19104, USA*
[14]*Physics Department, Carleton University, Ottawa, Ontario, Canada*
[15]*Technische Universität München, Physikdepartment and Excellence Cluster Universe, Garching, Germany*
[16]*Department of Physics, University of Seoul, Seoul, Korea*
[17]*Waste Isolation Pilot Plant, Carlsbad, New Mexico 88220, USA*
[18]*Kellogg Lab, Caltech, Pasadena, California 91125, USA*

(Received 27 June 2013; revised manuscript received 23 November 2013; published 28 January 2014)

We report on an improved measurement of the $2\nu\beta\beta$ half-life of ^{136}Xe performed by EXO-200. The use of a large and homogeneous time-projection chamber allows for the precise estimate of the fiducial mass used for the measurement, resulting in a small systematic uncertainty. We also discuss in detail the data-analysis methods used for double-β decay searches with EXO-200, while emphasizing those directly related to the present measurement. The ^{136}Xe $2\nu\beta\beta$ half-life is found to be $T_{1/2}^{2\nu\beta\beta} = 2.165 \pm 0.016(\text{stat}) \pm 0.059(\text{sys}) \times 10^{21}$ yr. This is the most precisely measured half-life of any $2\nu\beta\beta$ decay to date.

DOI: 10.1103/PhysRevC.89.015502 PACS number(s): 23.40.−s, 21.10.Tg, 14.60.Pq, 27.60.+j

I. INTRODUCTION

Nuclear $\beta\beta$ decay is a well-known second-order weak transition that may occur in a number of even-even nuclei. The two-neutrino decay mode ($2\nu\beta\beta$) has been directly observed in nine nuclei with half-lives ranging between 10^{18} and 10^{21} yr [1–4], and half-lives as long as 10^{24} yr have been established indirectly through radiochemical and geochemical means (see Ref. [2] for a review). Following Ref. [5], the $2\nu\beta\beta$ half-life $T_{1/2}^{2\nu}$ can be related to the nuclear matrix element $M^{2\nu}$ and the known phase-space factor $G^{2\nu}$ according to

$$\frac{1}{T_{1/2}^{2\nu}} = G^{2\nu} g_A^4 m_e^2 |M^{2\nu}|^2, \tag{1}$$

where $g_A = 1.2701$ and m_e is the mass of the electron. We see from Eq. (1) that measurements of $2\nu\beta\beta$ half-lives effectively measure the $M^{2\nu}$ matrix elements for $\beta\beta$ source isotopes.

The interest in $\beta\beta$ decay is, of course, largely driven by the possibility of discovering lepton-number violation via

*Also at SNOLAB, Sudbury, ON, Canada.
†Corresponding author: michael.marino@mytum.de
‡Now at Yale University, New Haven, CT, USA.
§Now at Air Force Technical Applications Center, Patrick AFB, FL, USA.
¶Also at TRIUMF, Vancouver, BC, Canada.
‖Now at SRI International, Menlo Park, CA, USA.

the exotic neutrinoless mode ($0\nu\beta\beta$). The observation of the $0\nu\beta\beta$ decay would profoundly alter our understanding of the neutrino sector by demonstrating the Majorana nature of neutrinos and by providing information about the absolute scale of the neutrino mass spectrum.

Perhaps the simplest and most promising mechanism for the $0\nu\beta\beta$ mode is the virtual exchange of light but massive Majorana neutrinos. The half-life for the neutrinoless mode, when mediated by such massive Majorana neutrino exchange, is given by

$$\frac{1}{T^{0\nu}_{1/2}} = G^{0\nu}|M^{0\nu}|^2|\langle m_{\beta\beta}\rangle|^2, \tag{2}$$

where $G^{0\nu}$ is the phase-space factor, $M^{0\nu}$ is the nuclear matrix element, and $\langle m_{\beta\beta}\rangle$ is the effective neutrino mass. While the $G^{0\nu}$ are known for all nuclei of interest, the corresponding nuclear matrix elements need to be calculated and have a substantial theoretical uncertainty [6]. Because the experimental data are available across a variety of complex nuclei, measurements of $2\nu\beta\beta$ half-lives provide an important challenge to all types of nuclear structure models and thus also to their ability to correctly evaluate the $M^{0\nu}$ matrix elements. Moreover, some authors have argued that, although the physics of the two $\beta\beta$ decay modes are quite different, measurements of the $2\nu\beta\beta$ half-lives can constrain the particle-particle coupling constant g_{pp} within the quasiparticle random-phase approximation (QRPA) [7]. This mitigates theoretical instabilities and uncertainties.

The $M^{2\nu}$ matrix elements are perhaps even more difficult to evaluate theoretically than $M^{0\nu}$ because the momentum transfer in $2\nu\beta\beta$ decay is comparable to the typical Q value involved, whereas for $0\nu\beta\beta$ decay it is, on average, considerably larger. As a consequence, the $M^{2\nu}$ of the various nuclei are known to vary by up to an order of magnitude, whereas the $M^{0\nu}$ appear to be rather similar to each other. As a result, establishing or substantially constraining the $0\nu\beta\beta$ decay rate in a given nucleus allows one to project the corresponding rate in other nuclei.

Apart from these physics considerations, precise determinations of the $2\nu\beta\beta$ half-life, such as the one reported here, provide, to a large extent, a validation of the techniques that are also used for the measurement of the $0\nu\beta\beta$ decay and the exceedingly low backgrounds obtained in today's experiments.

Among the several isotopes being most actively pursued for $\beta\beta$ experiments at the multikilogram scale and beyond, ^{136}Xe was the last to have its $2\nu\beta\beta$ decay observed [3,4], in part because its small matrix element leads to a long half-life. In this article we report on a substantially improved measurement of the $2\nu\beta\beta$ half-life of ^{136}Xe by the EXO-200 experiment. EXO-200 has published results from two data sets, the first collected between May 21, 2011, and July 9, 2011 (Run 1), and the second collected between September 22, 2011, and April 15, 2012 (Run 2a). Run 1 data produced the first measurement of the $2\nu\beta\beta$ half-life of ^{136}Xe [3], while Run 2a data placed a new limit on the existence of the $0\nu\beta\beta$ decay [8] in substantial tension with the observation claim reported in Ref. [9]. These results have been confirmed and complemented by KamLAND-Zen [4,10].

In the interim period between Run 1 and Run 2a the EXO-200 front-end electronics were improved, the lead shield was completed, and the electronegative impurity content of the xenon was reduced by a factor of ten. Because of these improvements, the results presented in this article are based upon the more powerful Run 2a data set and take advantage of significant additional improvements to the event reconstruction methods, the Monte Carlo simulation, and a greater understanding of the detector response and behavior acquired since the publication of Ref. [8].

II. DETECTOR DESCRIPTION

A. EXO-200 detector

The EXO-200 detector has been described in detail elsewhere [11]. Here we review those features of the detector which are of particular relevance for the measurement of the $2\nu\beta\beta$ decay rate. We give special attention to the detector geometry, readout scheme, and shielding.

The centerpiece of the experiment is a liquid xenon (LXe) time-projection chamber (TPC), as shown in Fig. 1. The EXO-200 LXe is enriched to $80.672\% \pm 0.14\%$ in ^{136}Xe (Sec. IX C 5), with the balance being composed mostly of ^{134}Xe. LXe is a good ionizing radiation-detection medium because it produces substantial ionization and scintillation signals. The LXe is housed in a cylindrical copper vessel of length ∼44 cm and diameter ∼40 cm and is instrumented by two back-to-back TPCs that share a common cathode at the center of the vessel. The end caps of the vessel host identical detector packages, each of which consists of two crossed and segmented wire grids and an array of large area avalanche photodiodes (APDs) [12].

Energy deposits in the LXe produce free ionization charge and scintillation light (at 178 nm). The charge drifts along

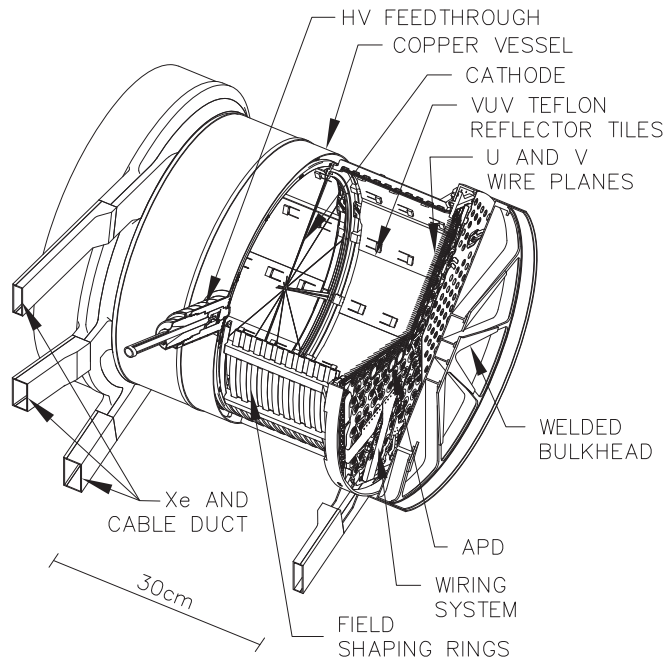

FIG. 1. Cutaway view of the EXO-200 TPC.

the axis of the detector towards the nearest end cap under the action of a uniform electric field, and the scintillation light is collected and measured by the APD arrays. Because the cathode has an optical transparency of 90% (at normal incidence), the scintillation light is detected simultaneously by both APD arrays while the ionization is detected only in the TPC in which it was produced.

When drifting ionization reaches the end cap detector package, it passes through the first wire grid, known as the shielding grid or induction grid, and is collected by the second wire grid, which acts as the anode (see Fig. 5). The shielding grid lies 6 mm in front of the anode, while the APD array lies 6 mm behind it. Both grids are segmented and read out by charge-sensitive preamplifiers. The amplitude of the charge-collection signal on the anode wires measures the ionization energy. Because the grids are crossed at an angle of 60°, the anode and the induction signals give measurements of two correlated spatial coordinates, which we refer to as U (anode coordinate) and V (induction coordinate). We transform these coordinates into an orthogonal X-Y coordinate system, as illustrated in Fig. 2. We refer to the anode as the U-wire system and the induction grid as the V-wire system.

The Z coordinate of the charge deposition (along the axial direction of the detector) is inferred from the product of the drift velocity and the drift time, where the start time is given by the prompt scintillation signal. The drift velocity is found to be 1.71 mm/μs (see Sec. VIII C), which agrees within 10% with previous measurements [13] at this drift field (374 V/cm from a three-dimensional simulation). This field is achieved by setting the cathode, V-wire, and U-wire voltages to −8.0 kV, −780 V, and virtual ground, respectively, while the front face of each APD array is biased to ∼(−1400 V). This arrangement gives an electric field of 778 V/cm between the U and V wires, which is sufficient to ensure 100% charge transparency of the V wires.

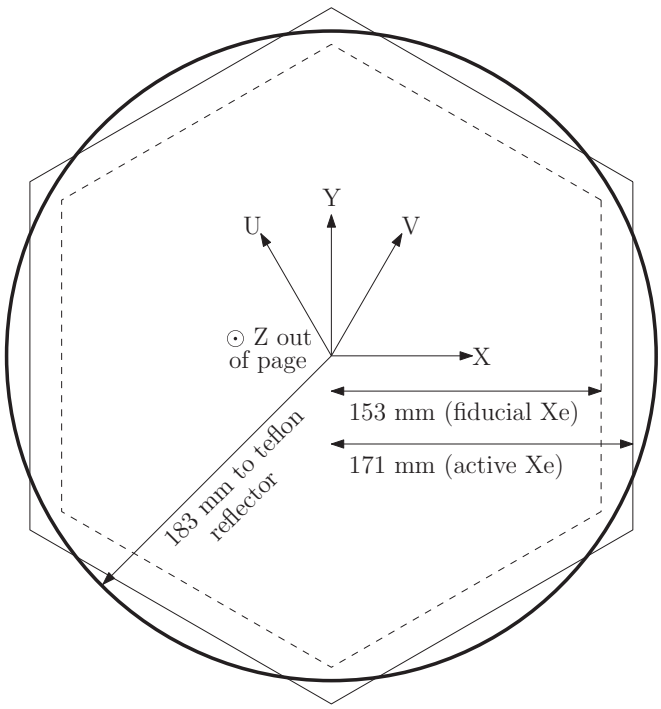

FIG. 2. Diagram of the EXO-200 U-V-Z and X-Y-Z coordinate systems. Also shown are the hexagonal active region and fiducial region and the circular projection of the Teflon reflector panels.

To reduce the channel count and attendant cabling mass, each wire grid is composed of 38 wire triplets that were fabricated by photoetching phosphor bronze sheet metal. Individual wires in each triplet have a roughly diamond-shaped cross section with a full width of about 130 mum. The wire pitch is 3 mm, and because the wires are ganged in groups of three, charge readout channels have a 9-mm pitch, for a total grid width of 342 mm. The wire triplets are mounted on acrylic beams that are connected to form a hexagonal shape. The optical transparency of each grid is 96% at normal incidence.

The distance from the U wires to the cathode is 198 mm, giving a maximum charge drift time of 115.5 μs (see Sec. VIII C). Each TPC has ten field-shaping copper rings mounted on acrylic "combs" which step down the cathode voltage to the V wires and which ensure a uniform drift field in the bulk of the LXe. The voltage grading is achieved by a string of custom low-radioactivity 900-MΩ resistors. The inner side of the field rings and the resistor package are covered by 1.6-mm-thick PTFE (Teflon) tiles capable of reflecting the 178-nm scintillation light.

Each detector package is backed by an APD array composed of 234 unencapsulated silicon devices produced for EXO-200 using selected materials. Each device is circular with a diameter between 19.6 and 21.1 mm and an active diameter of 16 mm. The APDs are mounted in two hexagonal-shaped copper platters which provide a common bias voltage to the APD cathodes of −1400 and −1380 V on the two detector sides. The APD anodes are provided a trim voltage, near ground, by their preamplifiers. The devices are hexagonally packed such that the sensitive area of each platter is 48% of the total end-plate area. The interior side of each platter is covered by vacuum-deposited aluminum and MgF_2 to reflect VUV scintillation photons that do not strike the sensitive areas of the APDs. In each array one APD device is replaced with a PTFE diffuser that can be illuminated by an external laser pulser with a wavelength of 405 nm fed through optical fibers. This allows the response of the APD arrays to be periodically monitored. Reference [12] describes the testing, performance, and selection of the APDs. The gain curve, noise, and relative quantum efficiency for each APD device was measured at LXe temperature as a function of bias voltage, and devices with similar gain characteristics were grouped together. The typical grouping is a gang of seven, although other groupings are also used. Each APD gang is monitored by a single charge-sensitive preamplifier to reduce cabling material. The anode voltages of the gangs can be trimmed by as much as 100 V in groups of six channels. This allows the gains of the APD channels to be matched to within 2.5% with a nominal gain factor of 200. Each APD has a capacitance of 125 pF when biased at ∼(−1400 V), for a channel capacitance of about 1 nF. This leads to substantial but tolerable electronic noise in the front end (three gangs are disconnected owing to excessive leakage current).

The charge-sensitive preamplifiers for all three systems (U wires, V wires, and APDs) operate at room temperature outside the TPC and are connected to the detector by thin copper-clad polyimide flat cables. The flat cables penetrate into the xenon volume through custom-made epoxy seals.

The TPC vessel is fabricated from low-radioactivity copper and sealed via electron beam and TIG welding. To minimize the mass of the vessel, most of the copper is only 1.37 mm thick with stiffening features to bolster its mechanical robustness. We operate the TPC vessel at a nominal overpressure of 8.1 kPa, and changes of more than 5.3-kPa activate a feedback system that restores the operating point by either removing or adding xenon. On the rare occasions when this occurs, the radon level and purity level of the xenon may be temporarily affected. To achieve and maintain good xenon purity with respect to electronegative contaminants such as oxygen and water, the xenon is continuously recirculated through two heated zirconium getters located outside the detector. Because the getters must act on the xenon in the gaseous phase, the LXe is evaporated, driven through the purifiers with a custom-designed xenon gas pump [14], recondensed outside and above the detector, and returned to the detector inlet through a vacuum-insulated transfer line. We find that the purity of the LXe is closely correlated with the operation of this recirculation loop (see Sec. V C 2).

The installation of the detector is shown in Fig. 3. The TPC vessel is surrounded by a $\geqslant$50-cm-thick thermal bath of HFE-7000 cryofluid [15], which maintains the temperature of the TPC and which shields the detector from external γ radiation. The HFE-7000 is housed in a double-walled vacuum-insulated cryostat composed of two nested copper vessels fabricated from low-radioactivity copper plate of 27 mm thickness. The outer cryostat is surrounded in all directions by at least 25 cm of lead. The cryostat features a copper guide tube that allows radioactive sources to be inserted past the lead shield and into the cold HFE volume near the detector. ^{137}Cs, ^{60}Co, and ^{228}Th sources of various intensities are available for deployment.

The entire assembly is located in a class 100 clean room that is surrounded on four of six sides by a cosmic ray veto system. The veto system consists of 29 5-cm-thick Bicron BC-412 plastic scintillator panels obtained from the concluded KARMEN neutrino experiment [16]. Each panel is observed by eight photomultiplier tubes (PMTs) and is supported by 4 cm of borated polyethylene. The clean-room laboratory is installed underground at the Waste Isolation Pilot Plant near Carlsbad, New Mexico, USA, providing 1585 m water equivalent of overburden [17].

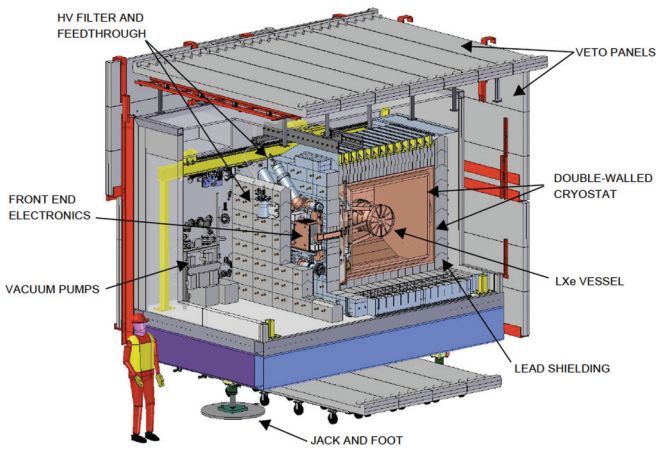

FIG. 3. (Color online) The EXO-200 installation at the Waste Isolation Pilot Plant.

An extensive materials-screening and cleanliness campaign, described in Refs. [11,18], was conducted during the design and construction phase of the experiment to ensure that the radioactivity of the detector would be suitable. Virtually all detector components inside the lead shield were custom fabricated for EXO-200. This effort was informed by a detector Monte Carlo simulation which predicted the background impact of each detector component. The enriched xenon itself was screened for noble gas and electronegative contaminants as described in Ref. [19].

B. Data acquisition

The fast data-acquisition (DAQ) system for the EXO-200 detector integrates the readout of 226 hardware channels (76 U-wire signals, 76 V-wire signals, and 74 APD gang signals), muon veto panel output, and a high-voltage (HV) glitch detector into a single data stream. The veto system triggers asynchronously from the TPC when both instrumented ends of a panel record a hit within a 1-μs coincidence time window. The HV glitch detector monitors high-voltage transients with $\sim\mu$s duration.

Each TPC hardware channel is initially coupled to the DAQ via front-end electronics, consisting of a low-noise charge amplifier with a dual, two-stage (integration and differentiation) shaper followed by a 12-bit, 1 MS/s analog-to-digital converter. The particular values of the shaping times vary according to the type of channel (e.g., APD, U, or V). The digitized data are fed to a trigger electronics module (TEM), which synchronizes the data from all hardware channels and forms detector triggers. The TEM also incorporates data from the muon veto panels and the HV glitch detector.

For the muon veto, the 2 light-readout channels for each panel, each instrumented with four PMTs, are fed into a discriminator module, which supplies a bit pattern of the panels above threshold. For a valid muon trigger, both ends of any one panel are required to be simultaneously above threshold to reduce the random trigger rate. A secondary, ADC/TDC-based electronics system is available, allowing the monitoring of panel stability with detailed semiannual ^{60}Co source calibration scans of the panels.

In the case of a trigger condition, data are written from the TEM to a control computer to be stored on disk. Muon veto or glitch detector events only initiate transfers of those particular types of records; these are later synchronized with TPC data by means of their time stamps. If a TPC trigger occurs, the TEM transfers digitized data for all 226 hardware channels for sample times starting 1024 μs before the trigger and ending 1024 μs after it. During a normal physics run, there are four types of TPC triggers used, with rough thresholds noted in parentheses: (a) individual U-wire trigger for LXe γ and β events ($\sim$100 keV), (b) APD individual trigger for activity

inside the respective APDs (∼3–4 keV), (c) APD sum trigger for LXe α events (∼25 000 photons), and (d) solicited (forced) trigger at 0.1 Hz, for monitoring detector performance. Further information on the DAQ system may be found in Ref. [11].

C. Data-processing structure

The processing of data follows a tiered scheme for each run.

(1) Tier 0 → Tier 1, "rootification": conversion of binary data files to ROOT [20] files; low-level verification of data validity.
(2) Tier 1 → Tier 2, "reconstruction": first two reconstruction stages (see Sec. IV); noise and muon taggers; calculations of waveform characteristics.
(3) Tier 2 → Tier 3, "processing": final reconstruction stage ("clustering") (see Sec. IV D); data corrections (e.g., gain, grid, and purity) (see Sec. V).
(4) Tier 3 → standard analysis scripts, "trending": extraction of parameters from a run (e.g., noise, threshold, etc.) useful for tracking trends over time.

D. Data-analysis strategy

As expected from the materials-screening campaign, we find in the data that the primary backgrounds to $2\nu\beta\beta$ in EXO-200 are γ and β interactions owing to trace quantities of ^{40}K, ^{232}Th, and ^{238}U in the detector materials. We separate these backgrounds from $2\nu\beta\beta$ candidates by taking advantage of the detector's good energy and position resolution and its ability to perform pattern recognition. First, we label an event as being "single-site" (SS) if it is consistent with having all charge deposits confined to a single volume with a characteristic dimension of ∼2–3 mm, as expected for most $2\nu\beta\beta$ events in LXe. Otherwise, the event is labeled as "multi-site" (MS). Owing to the predominance of the Compton scattering process in the energy range of interest (700 to 3500 keV), γ events are mostly categorized as MS as they commonly produce two or more localized charge deposits separated by at least several centimeters in LXe. Second, we calculate for each event the "standoff distance," or the shortest distance between the various charge depositions to an anode wire or reflector suface. γ events and $2\nu\beta\beta$ events have distinguishable standoff probability distributions because the latter are uniformly distributed in the LXe, whereas the former tend to originate in the passive detector materials and exhibit some attenuation in a detector of the size of EXO-200. Third, we measure the total energy of each event by combining the charge and scintillation signals in a manner which takes advantage of the anticorrelation between these channels to improve the energy resolution [21]. This last procedure is essential for the search for $0\nu\beta\beta$, where the signal is a resolution-limited feature at the Q value, but is also utilized in the present measurement of the $2\nu\beta\beta$ decay.

We exploit these three variables by selecting fiducial β-like events in the data, dividing them into the SS and MS categories, and performing a simultaneous maximum-likelihood fit to the energy spectra and standoff distance of both event samples. The probability distribution functions (PDFs) provided to the fit are determined by a Monte Carlo simulation of the relevant signal and background sources. This strategy is validated by comparing data and simulation for calibration sources of known activity that are periodically inserted near the detector. The efficiency of the event selection for $2\nu\beta\beta$ events is determined by a combination of data and Monte Carlo studies and is cross checked by the external calibration source data.

In the following we describe the Monte Carlo simulation (Sec. III), event reconstruction (Sec. IV), calibration and energy measurement (Sec. V), simulation-measurement agreement (Sec. VI), data quality selection (Sec. VII), event selection cuts (Sec. VIII), and likelihood fits and $2\nu\beta\beta$ half-life measurement (Sec. IX).

III. MONTE CARLO SIMULATIONS

The EXO-200 Monte Carlo simulation software is split into two independent components. The first component, developed within the GEANT4 simulation package [22], parametrizes the geometry of the EXO-200 detector and surroundings. The second stage uses the output from the first component—energy depositions within the simulated detector—to calculate electronic signals. The data format produced by this process is identical to that of real data and may be processed through the Tier 1 and Tier 2 reconstruction and analysis chains described in Secs. II C and IV.

A. Simulated geometry

The simulated geometry implements a detailed description of the TPC and its internal components and includes the surrounding HFE, cryostat, and lead shield. Three-dimensional computer-aided design (CAD) models of the detector are used and coded using GEANT4 shape primitives, as illustrated in Fig. 4 for the copper components of the inner detector. An approximate geometry is used for the shape of some complex components, so a check is made to verify that the mass of materials is accurately reproduced, as shown in Table I for the materials shown in Fig. 4.

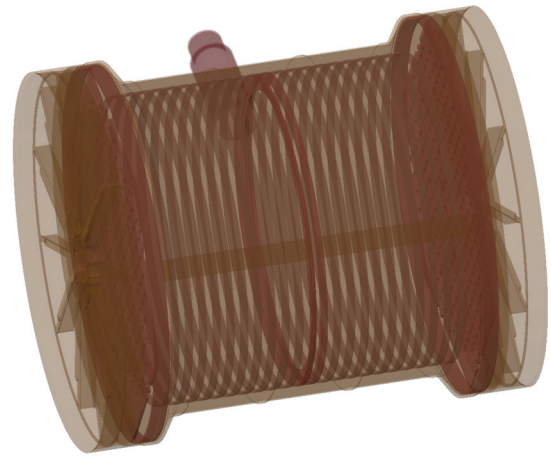

FIG. 4. (Color online) Visualization of the simulated TPC vessel and internal copper components.

TABLE I. Comparison between copper mass in the detector CAD model and the GEANT4 model. The two models have independent implementations, and differences are understood to be attributable to simplifications in the GEANT4 geometry. Although these distinctions could lead to minor differences in γ attenuation between data and simulation, this effect is expected to be small and is cross checked by external γ calibration source data (see Sec. VI).

Component	Quantity	CAD mass (kg)	GEANT4 mass (kg)
Outer cryostat	1	3453	3364
Inner cryostat	1	2843	2575
Total cryostat		6296	5939
Source tube	1	0.533	0.207
TPC leg	1	6.979	6.944
HV feed	1	0.491	0.303
LXe vessel	1	22.36	22.32
APD frame	2	3.144	4.440
Wire support Ring	2	2.659	1.468
Field ring	20	3.055	3.240
Cathode ring	1	0.721	0.728
Dummy Cathode ring	1	0.323	0.327
Total TPCs		32.753	32.826

B. Simulated signal generation

The signal calculation for wire channels employs a two-dimensional (2D), simplified geometry which assumes that U wires and V wires are parallel to one another, infinitely long, and perpendicular to the plane of calculation. In addition, in this configuration the V wires lie directly above the U wires in the Z direction. For this setup the weighting potential, $\phi(\vec{x})$, and electric field, $\vec{E}(\vec{x})$ have been calculated using Maxwell 2D [23], which allows one to model drifting charge at any location in the detector and calculate the resulting induced signal using the Shockley-Ramo theorem [24]. In this method, the charge induced on a wire by the movement of charge, q, from $\vec{y}_0$ to $\vec{y}$ is given by $q[\phi(\vec{y}) - \phi(\vec{y}_0)]$, where ϕ is the weighting potential for the particular wire. The weighting potential for a single U-wire channel along with example charge drift trajectories are shown in Fig. 5. Charge diffusion during the drift is not modeled in this calculation. This does not significantly affect the quality of the simulation because the larger effect of transverse charge diffusion in LXe at the field used here (see, e.g., [25]) produces an rms spread of $\sim$2 mm to be compared with the 9-mm-wire readout pitch. The effect of longitudinal diffusion was observed when taking low-electric-field data as it lengthened the U-wire pulse rise time. However, this effect becomes negligible at the nominal electric field. Once signals are calculated, they are shaped with the appropriate channel transfer function. For Monte Carlo simulation production runs, white noise is added to the signal waveforms, though there exists the possibility to add real noise using event traces from solicited triggers.

To determine if the 2D geometry is a valid approximation to use, waveform characteristics were calculated and compared

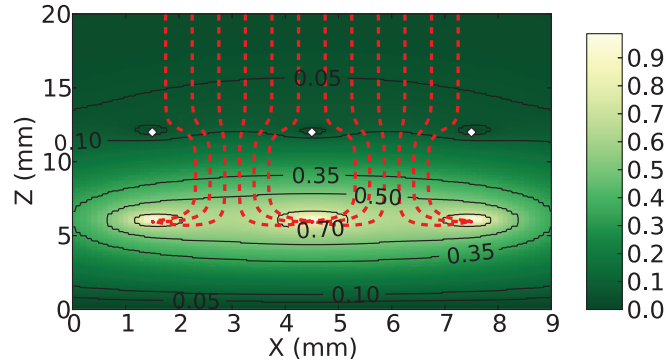

FIG. 5. (Color online) The magnitude of the calculated weighting potential for a single U-wire readout channel. The weighting potential peaks to one at the positions of the three wires composing a signal channel ($X = 1.5$, 4.5, 7.5 mm, $Z = 6$ mm). Example charge drift trajectories are shown by the overlaid red dashed lines; deflections of the trajectories arise from the presence of a V-wire channel (diamonds at $X = 1.5$, 4.5, 7.5 mm, $Z = 12$ mm) situated directly above the U-wire channel.

for simulated wire signals and for data from a ^{228}Th source run. In particular, the rise time of the pulses and the time difference between maximum and minimum are calculated (see Sec. IV C 2). The results of this study are shown in Fig. 6, where it is clear that signal generation well reproduces the distributions from data.

In addition, a fully three-dimensional (3D) COMSOL [26] finite element calculation was used to produce a 3D electric field and weighting potentials for the 76 wire channels populating a single TPC at the proper 60° angle between U and V grids. Although this model is currently too slow to be used in Monte Carlo simulation production runs, calculations from it have been used during fiducial volume studies of the detector, in particular to help understand regions near the edge of the wire grid where the field configuration is complex. Results from a similar study of waveform characteristics of traces generated from this model are included in Fig. 6. A comparison of the two calculations shows the 2D model to provide a valid approximation of the charge collection.

The signal generation for APD channels uses a parameterized light response function which returns the expected amount of light hitting both APD planes given a charge deposition at a given location in the detector. The light response function was derived from a Monte Carlo study of light collection in the TPC which included geometric factors, reflectance, and scattering. Effects from the anticorrelation between the ionization and scintillation (see Sec. V D) are not simulated. The resulting unshaped APD pulse shapes are assumed to be step functions, a valid assumption given that the integration time of the APD electronics transfer function ($\sim$1 μs) is much longer than the intrinsic APD rise time (10–100 ns). As with U and V wires, these unshaped pulses are transformed with the appropriate electronics transfer functions and white noise is added.

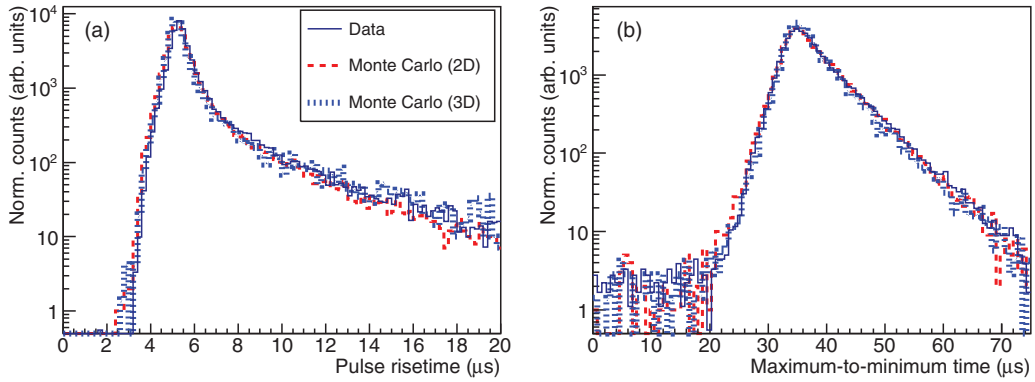

FIG. 6. (Color online) Comparison of the distributions of the pulse rise time (a) and maximum-to-minimum time (b) on U wires between calibration data and simulations using 2D and 3D field maps (see Sec. IV C 2) for ^{228}Th data. The long tail in the rise-time distribution is attributable to Compton scatters. Only wire signals above 200 keV are compared, as the values of rise time and maximum-to-minimum time for low-amplitude signals depend strongly on the waveform noise profile. The distributions are normalized to the same total number of events for comparison.

IV. EVENT RECONSTRUCTION

Event reconstruction is the process by which waveforms are analyzed to derive information such as energy content and topology of events. The reconstruction of an event has three stages:

(1) signal finding;
(2) signal parameter estimation;
(3) clustering, or assembling of found signals to determine event topology.

The following terminology is used in this section: a "signal" refers to a hit that is reconstructed on a particular channel, a "bundle" is a group of signals from a single channel type, and a "cluster" is a set of bundles that have been associated together to determine the event position.

A. Signal models

Signal-shape templates are used extensively in reconstruction in both the signal-finding and parameter-extraction stages and are produced for all channels. In the case of U and V wires, unshaped signals are generated using the signal simulation described in Sec. III B. A simple step function is used for APD channels. Unshaped waveforms are then filtered using the appropriate transfer function to create the final signal template shape for a given channel. Transfer functions are defined by the front-end electronics (see Sec. II B), resulting in three differentiation (one stage from the preamplifier) and two integration stages. The values for these stages for each channel type are given in Table II. It is important to note that the value of the third differentiation stage of the U wires is a measured parameter and varies for each U-wire channel. Using the measured value for each channel was found to improve the fits used to determine signal heights (Sec. IV C), which lead to an improved detector resolution.

TABLE II. Shaping times (all in μs) relevant to the transfer functions of different channel types. The third differentiation stage for the U-wire signals is measured for every channel by fitting to pulse shapes from charge injection data.

Channel type	Stage type				
	Integration		Differentiation		
APDs	3	3	10	10	300
U wires	1.5	1.5	40	40	51–85 (nominal 60)
V wires	3	3	10	10	60

B. Signal finding

It is necessary to search for signals on waveform traces because they are not always guaranteed to arrive at a given time (e.g., specified by a trigger). Two methods are used to find signals on waveform traces: applying a matched filter and waveform unshaping. The second method is used to identify pulses closely following one another within a signal found by the matched filter.

1. *Matched filter*

A matched filter is used to find signals owing to its simple algorithmic implementation and because it has been observed to produce stable performance over time in varying noise conditions. The filter (see, e.g., Ref. [27]) is applied in Fourier space,

$$y(t) = \mathfrak{F}^{-1}\{X(f)H^*(f)\}, \tag{3}$$

where $y(t)$ is the filtered signal, $\mathfrak{F}$ is the discrete Fourier transform (FT), $X(f)$ is the FT of the original waveform, $x(t)$, and $H^*(f)$ is the complex conjugate of the FT of the transfer function, $h(t)$, for the particular channel. For APD channels, Eq. (3) is further divided by the noise spectrum of the channels to whiten the spectrum. This is *not* performed for U-wire channels as the additional division was found to broaden the signal owing to the longer U-wire shaping times, detrimentally affecting subsequent peak finding. V wires also have no additional noise division.

U- and V-wire channels are filtered by applying the template model defined for each respective channel. APD

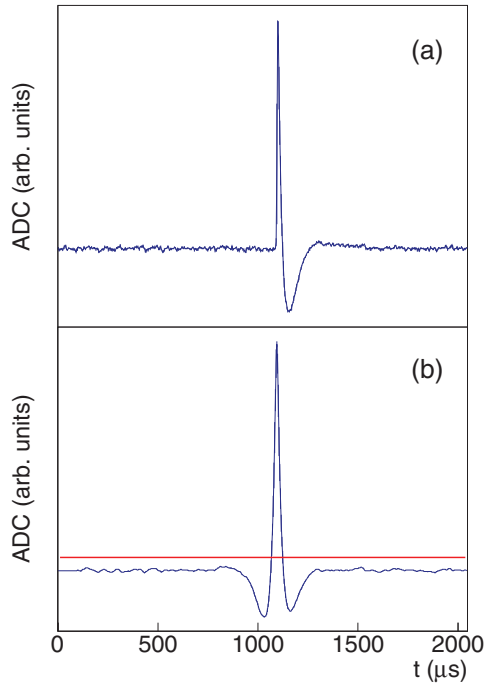

FIG. 7. (Color online) A U-wire waveform (a) and the result of the matched filter (b). The horizontal line in (b) is the calculated threshold.

channels, in contrast, are first assembled into two sum waveforms generated by summing together the waveforms from all channels on each APD plane. This results in two waveforms, each of which is then filtered using Eq. (3) with the APD transfer function. An example of a waveform before and after filtering is shown in Fig. 7. A peak-search algorithm is performed on the filtered waveforms, looking for amplitudes exceeding a certain threshold. This threshold is calculated for each waveform on an event-by-event basis to reduce the sensitivity to channel- and time-based noise variations. The algorithm proceeds by first determining the mean absolute deviation (MAD) of the waveform from its baseline, removing all parts of the waveform exceeding $(3\sqrt{\frac{\pi}{2}}) \times$ MAD, and then recalculating the MAD. This is equivalent to removing values greater than 3σ if the deviations from the baseline are normally distributed. The threshold is defined as 5 (4) times this final MAD for wire (APD) signals.

2. *Waveform unshaping*

Because the matched filter is designed to find single pulses, it is ill suited to disentangle multiple signals on a single trace when these signals arrive close to one another in time. Hence, a dedicated algorithm is applied to the original waveforms after they have been identified by the matched filter. This algorithm "unshapes" the signal, obtaining the original charge deposited $q(t)$,

$$q(t) = \mathfrak{F}^{-1}\{H^{-1}(f)X(f)\}, \tag{4}$$

with the same definitions as given for Eq. (3), where $H^{-1}(f)$ is the inverse transfer function. This process is very sensitive to inaccuracies of the transfer function used owing to inexact pole-zero cancellation. Detailed studies show that the procedure works best on a short (265 μs) interval centered around the pulse time found by the matched filter. $q(t)$ is subsequently reshaped with a 2-μs triangular, or moving average, filter (see, e.g., Ref. [28]). The reshaped waveform is then analyzed with a peak-search algorithm to determine the presence of any additional signals.

C. Parameter estimation of signals

1. *Amplitude measurement*

The amplitudes of all U-, V-, and APD sum signals are measured by fitting the waveforms to their respective signal models (see Sec. IV A). A χ^2 function is built using the signal model, the data, and the output of the previous signal-finding stage,

$$\chi^2 = \sum_{l=0}^{L} \frac{\left[x_l - b - \left(\sum_{i=0}^{N}\{A_i f_{\mathrm{SM}}(x_l,t_i)\}\right)\right]^2}{\sigma^2_{\mathrm{noise}}}, \tag{5}$$

where x_l is the data sample at time l, b is the measured baseline, i is the index of the N signals on the waveform, A_i and t_i are the amplitude and time of the ith signal, and f_{SM} is the signal model. The baseline and the rms noise σ_{noise} are calculated and fixed for each waveform. A_i and t_i are the only floating parameters, and the values estimated during the signal fitting stage are used as initial input. The size of the fit window, L, extends ± 40 μs around the signal (defined in the finding stage). In the case of U wires, the upper fit window limit is extended to 140 μs to include the longer undershoot induced by the larger differentiation times in the U-wire transfer functions. When multiple signals are found on the waveform traces, the fit windows are determined for each signal and combined. In the case of signals further apart than 40 (or 140) μs, several separated fit windows are produced. An example of fits to U and V waveforms is given in Fig. 8.

The χ^2 function is minimized using MIGRAD [29], resulting in signal amplitudes, times, and errors, in addition to the overall value of the minimized χ^2 function. Before the fitting stage is completed, the results of the fits to the two APD sum signals are used to then fit individual APD gang channels separately and extract the amplitudes of each gang channel. The t_i parameters from the fits to the two APD sum signals are used as input to Eq. (5), but these values are fixed during the subsequent fit; only the amplitude parameter(s), A_i, are allowed to float when fitting the gang signals.

2. *Waveform characteristics*

In addition to the pulse characteristics derived from the waveform fits, several metrics are calculated directly from the U-wire waveforms for use in pulse-shape-based discrimination between "collection" and "induction" signals. In this sense, we define induction signals on U wires as signals that occur when charge drifts close enough to a channel to induce a signal, but does not deposit on that channel. These induction signals must be corrected for so that they are not mistakenly reconstructed as a low-energy charge cluster (see Sec. IV D), causing a SS topology event to be interpreted as a MS event. This has particularly important implications for event classes

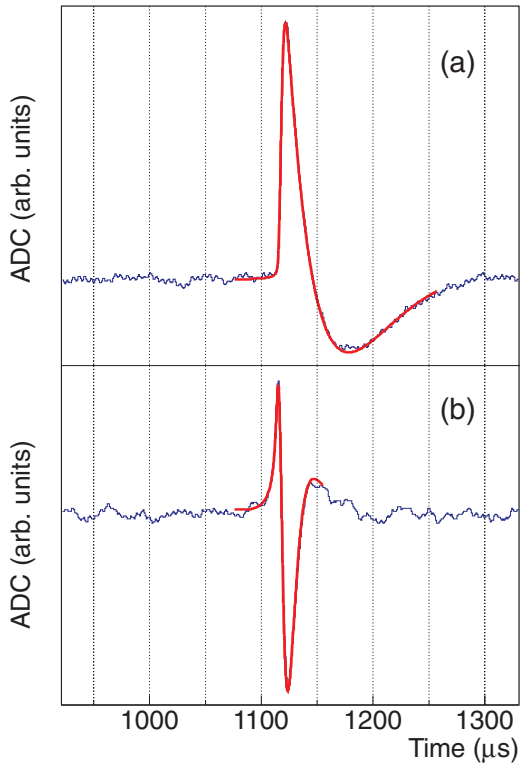

FIG. 8. (Color online) Examples of fits to a U wire (a) and V wire (b) on an expanded vertical scale. One can see that the V-wire peaks earlier than the U-wire signal.

that are predominantly SS (e.g., $0\nu\beta\beta$ and $2\nu\beta\beta$) and would be mistakenly classified as MS with a loss of efficiency.

The following discriminants are calculated.

(1) Pulse timing:
   (a) the rise time of the pulse, measured from the last time the pulse crosses a minimum threshold (set to 10% of the pulse height above the baseline) to the first time the pulse crosses a maximum threshold (at 95% of the pulse height above the baseline);
   (b) the time from the pulse maximum to the following pulse minimum, defined similarly as the time between the last crossing of a maximum threshold (90% of the pulse height, measured from the pulse minimum) and the first crossing of a minimum threshold (10% of the pulse height above the pulse minimum).

(2) Pulse integral: The pulses are unshaped using inverse transfer functions (see Sec. IV B 2), and the integral of the pulse is calculated in a window within 10 μs before and 40 μs after the pulse maximum.

(3) Fit χ^2: Following the standard fitting procedure for U-wire signals described in Sec. IV C, the same signal finding and fitting procedure is repeated for each U-wire waveform using a signal template describing a U-wire induction signal instead of the standard collection template. The fit χ^2 value is then calculated for fits to both the collection and the induction signal templates in a time window restricted to 20 μs before and 30 μs after the signal.

(4) Nearest-neighbor amplitude: For each U-wire signal, the total energy on neighboring channels within 50 μs is calculated (U-wire induction signals reconstructed as collection signals have poor time estimations owing to the template mismatch.)

Distributions of these discriminants are given in Fig. 9, comparing the values for induction signals and collection signals. A full discriminator is built from a combination of these values to ensure the collection efficiency for collection signals with at least 250 keV of deposited energy is >99.9%. With the chosen cut, the rejection efficiency for U-wire induction signals is 77%, integrated over the $2\nu\beta\beta$ energy spectrum. Because signals identified as induction by these selection criteria are required to have an energy deposit on a neighboring channel of >1000 keV, no events can be forced below the 700-keV analysis threshold owing to removal of misidentified collection signals. These efficiencies were calculated using Monte Carlo studies.

D. Signal clustering

Once the time and amplitude of signals on U, V, and APD channels have been found and properly gain corrected (see Sec. V B), these signals are grouped together to form 3D "clusters." Because signals from different channels arising from the same charge deposit will have correlated characteristics (e.g., amplitudes and times), these characteristics can be used to guide the clustering process that proceeds in a stepwise fashion. First, signals of like channels are associated together (U wires with other U wires, etc.) in a process called bundling. U-wire signals identified as owing to induction, using the criteria described in Sec. IV C 2, are ignored when constructing bundles. The Z positions of these bundles are then determined by associating them with APD bundles. Finally, these wire bundles are grouped together to form fully 3D reconstructed clusters.

1. Signal bundling

U-wire signals on adjacent channels arriving close in time (within 3.5 μs) are bundled together. The time of each bundle is defined by the amplitude-weighted average of the associated signals. V-wire signals are also bundled according to time, using the relationship

$$|t_i - t_0 - (2.97\ \mu\text{s/chan})\Delta V| \leqslant 4.5\ \mu\text{s}, \qquad (6)$$

where t_0 is defined by the V channel with the largest amplitude, t_i is determined from the V channel of interest, and ΔV is defined as the absolute channel number difference of the two signals. For example, for two V-wire signals occurring on channels 39 and 37, ΔV would be 2. This is because "outer" V signals are reconstructed earlier in time than the "central" (largest-amplitude) V signal and the arrival-time difference grows roughly linearly with the number of channels between the signal and the central signal. This occurs because the V-wire channels further from the drifting charge become shielded by the nearby wires as the charge nears the V-wire

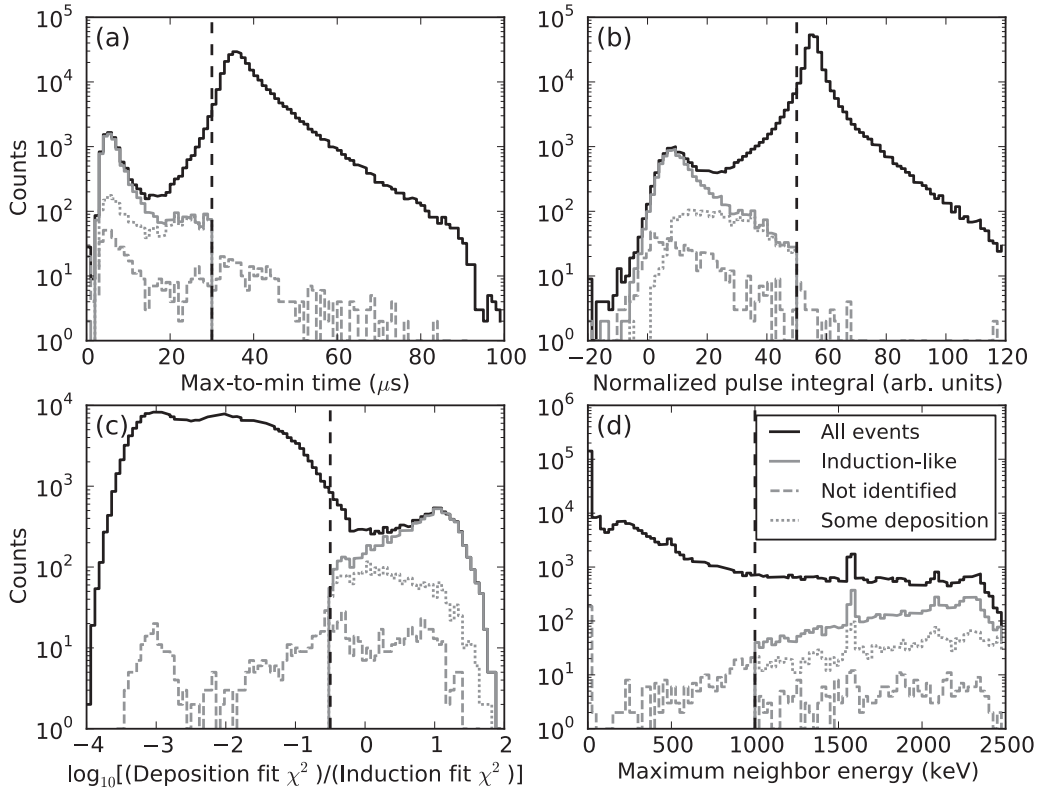

FIG. 9. Distributions of the discriminants described in the text used to identify induction signals, calculated for waveforms generated from ^{228}Th Monte Carlo simulations. The distribution of these values for all U-wire signals is shown as the solid histogram, with the cuts used for each value denoted by the vertical dashed lines. U-wire signals must satisfy *all* cuts to be identified as "inductionlike" signals. The cuts are chosen to ensure minimum impact on collection signals (acceptance efficiency >99.9%), corresponding to a rejection efficiency of induction signals of 77%, integrated over the $2\nu\beta\beta$ energy spectrum. Also shown are the distributions of simulated induction pulses which were *not* identified as inductionlike by the cuts ("Not identified") and simulated pulses containing at least some deposition, but which were identified as inductionlike ("Some deposition").

plane. In contrast to U-wire bundles, only the time of the *largest* V-wire signal is chosen as the time of the whole V-wire bundle; no weighted average is performed. Using the weighted time average in the V-wire bundle has been found to dilute the time correlation between U-wire and V-wire bundles.

The bundling of APD signals is performed solely based on time, associating signals if they arrive within 6 μs of one another, with the timing defined by the sum of the integration times in the APD electronics (see Table II). When multiple APD signals are grouped to form a scintillation bundle, the time of the scintillation bundle is calculated by performing the weighted average over the time and energy of the component signals.

2. Determining 2D position

A determination of the 2D event position is achieved by grouping together U- and V-wire bundles in their most likely configurations to generate charge clusters. The clustering stage employs PDFs that describe how likely it is that a particular U bundle is associated with a given V bundle. There are three PDFs to (1) describe the time difference between U and V bundles, (2) describe the consistency between the sum of signal amplitudes in the U and V bundles, and (3) ensure that the resulting (U,V) coordinate is physically allowed (not all U and V wires intersect one another because of the hexagonal shape of the grid frame). These PDFs are described in more detail in Sec. X.

The PDFs used to cluster U- and V-wire bundles together are dependent on the Z position of the U bundle. To calculate them, an associated scintillation bundle is found in the following way: From all scintillation bundles that occurred between 3 μs *after* and 3 μs plus the maximum drift time *before* the U-wire bundle, the one scintillation bundle with the *smallest* absolute time difference from the U-wire bundle is chosen. The expansion of the search window on both sides by 3 μs is again given by the integration times of the APD transfer functions. If no scintillation bundle lies in that time range, the Z position is set as undetermined and the particular U/V bundle will not be further clustered.

The negative natural log of the product of the three PDFs described above defines a test metric, the "cost," which is used as a measure of how well a U bundle matches a V bundle. This may be translated into an expression,

$$\text{cost} = \sum_{i=1,2,3} -\ln P_i, \tag{7}$$

where the sum is over the three PDFs. A lower cost indicates a better match, or a higher likelihood for a given configuration. The matching algorithm rigorously tests all combinations of the V and U bundles with one another, including whether multiple bundles of one type may actually correspond to a single bundle of the other type. The best matching configuration is the one for which the sum of the cost divided by the number of connections is minimal, where the number of connections is defined as the smaller of the number of U bundles or V bundles. Once this has been determined, a charge cluster is created for each of the connections within the matching configuration and each charge cluster is linked with its associated scintillation bundle.

It is possible that clustering fails to associate one or more of the U-, V-, or APD bundle types together, resulting in a cluster without full 3D position. This may occur owing to a clustering error or because signals are not found because they are below threshold. This produces an associated error on the $2\nu\beta\beta$ measurement, which is quantified in Sec. VIII D. It is also possible for clustering to skip an event completely if too many signals are found. This may introduce an error on the $2\nu\beta\beta$ efficiency if reconstruction mistakenly finds too many signals and these events are then ignored. However, the total number of skipped events is $<0.18\%$ of the final $2\nu\beta\beta$ counts. We choose to assign an additional 0.18% error on the $2\nu\beta\beta$ measurement to account for the possibility that events are mistakenly skipped by the clustering stage in reconstruction.

To determine the analysis threshold, the efficiency to find a signal on the three types of channels (U wire, V wire, and APD) was studied versus deposition energy. The three types of channels exhibit efficiencies with different dependencies on deposition energy, as well on position. An analysis threshold (700 keV) was chosen where all channel types demonstrated 100% signal-finding efficiency independent of the event deposition position.

V. CALIBRATIONS AND CORRECTIONS

A. TPC source calibrations

^{137}Cs, ^{60}Co, and ^{228}Th sources are utilized to calibrate the TPC response to γ radiation. The sources have been selected to span the energy range of interest. The source activities, listed in Table III, were chosen to collect calibration data quickly while not saturating the DAQ system. The ^{228}Th source is deployed every few days to a position near the cathode to monitor the electron lifetime and measure the energy response. Occasionally, all three sources are deployed in series to other positions around the TPC vessel for comprehensive calibration studies. These positions are shown in Fig. 10.

TABLE III. EXO-200 calibration sources. The activities shown here are referenced to September 1, 2009, and were verified by γ-ray spectroscopy within the collaboration. Other sources with greater activity are also available for deployment.

Source	Activity (Bq)	Half-life (yr)
^{60}Co	530 ± 6	5.27
^{137}Cs	2820 ± 33	30.1
^{228}Th	1417 ± 17	1.91

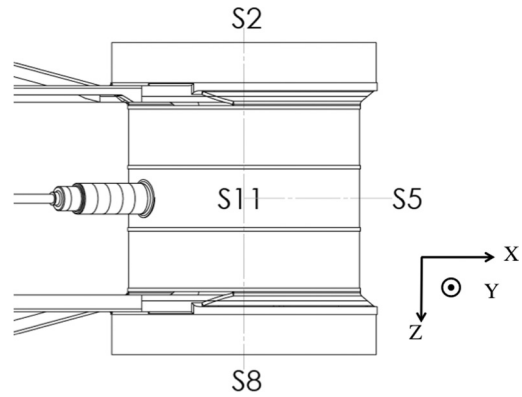

FIG. 10. The calibration source locations around the TPC vessel as viewed from above. The XYZ coordinates of the source locations are: S2 = (0.0, 0.0, −29.5 cm), S5 = (25.5 cm, 0.0, 0.0), S8 = (0.0, 0.0, 29.5 cm), and S11 = (0.0, 25.5 cm, 0.0). Not shown: S17 = (0.0, −25.5 cm, 0.0).

B. TPC channel-based corrections

The absolute U-wire channel gains were measured prior to Run 2a using a pulser coupled to the front-end electronics through a precision (1%) capacitor. The gain value, measured in units of electrons per ADC count, is calculated by a linear fit to the measured amplitude versus the injected charge. The stability of the gain values is monitored daily using a charge injection circuit which is integrated into the front-end card. This daily charge injection run is also used to monitor the time constant of the third differentiation stage of the preamplifier (see Table II).

The relative U-wire gain values are also determined with ^{228}Th source calibration data using the pair-production peak of 2615-keV γ's. The resulting channel-to-channel gain values are strongly correlated with those determined from the charge injection runs, as expected. The mean gain is ∼380 electrons/ADC unit, with 30% variation over all channels. The observed drift of the U-wire gains is $<1\%$ over the Run 2a data set, with $<0.1\%$ relative channel-to-channel drift. For the $2\nu\beta\beta$ half-life measurement the gain values determined from the pair-production peak are used.

The V wires are not directly used in the energy measurement, but variations in their relative gain can affect position reconstruction and clustering. We correct for these variations using the precision pulser charge injection data. The V-wire gains as determined from these calibrations are found to vary from 300 to 360 electrons per ADC count. These gain values are accurate within 2%–3%.

The APD channel gains are monitored periodically using the external laser pulser. The observed channel-to-channel gains vary by 12%, and the time variation is 1% over the Run 2a data set. However, for the $2\nu\beta\beta$ half-life measurement, the APD signals are not explicitly gain corrected on a channel-by-channel basis, as gain variations are absorbed in the light-map correction described below.

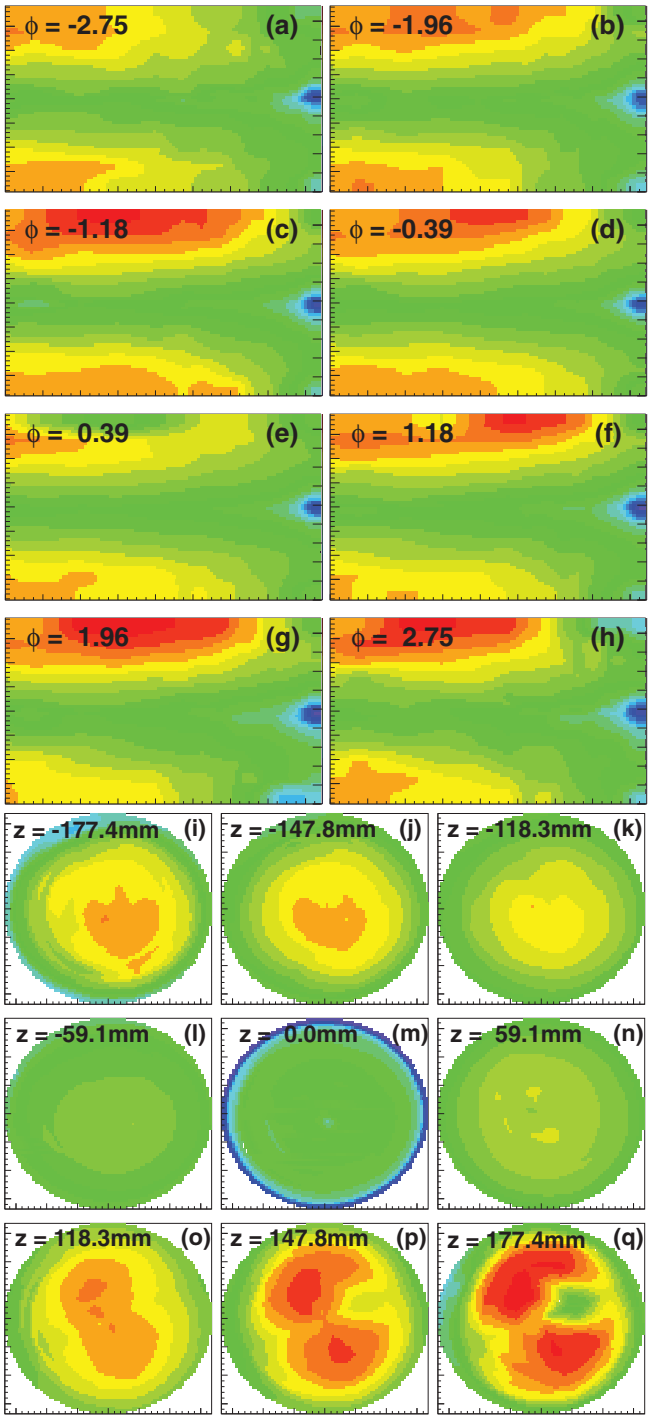

FIG. 11. (Color) The light response function $f(r,\phi,z)$ from September 22, 2011, until February 20, 2012, is shown here, indicated by the color coding. For both plots the correction factor ranges from 0.70 (blue) to 1.19 (red). Panels (a)–(h): The function evaluated at eight discrete values of the azimuthal angle ϕ over the full range of r (horizontal axis, 0 mm $< r <$ 168 mm) and Z (vertical axis, -192 mm $< Z <$ 192 mm). Panels (i)–(q): The function evaluated at nine discrete values of Z over the full range of X (horizontal axis, -168 mm $< X <$ 168 mm) and Y (vertical axis, -168 mm $< Y <$ 168 mm). A second response function (not shown here) is used from February 20, 2012, until April 15, 2012.

C. TPC position-based and time-based corrections

1. APD light map

The amount of scintillation light collected by the APDs depends on the location of the energy deposition. This variation is caused by differences in the solid angle covered by the APDs and by their gain differences. Three-dimensional correction functions are used to account for this position dependence. Such correction functions are generated from ^{228}Th calibration runs with the source placed at the two anodes and three positions around the cathode plane. The detector volume is divided into 1352 spatial voxels (13 radial bins, 8 azimuthal bins, and 13 Z bins). The bin widths are chosen to ensure adequate statistics, and to optimally map the response in the regions with a high light-collection gradient.

The light map is normalized such that the mean response is 1. A continuous correction function, $f(r,\phi,z)$, is created with a trilinear interpolation between the centers of the voxels in the light map.

Because maintenance was performed on the APD front-end boards in the middle of Run 2a, two light maps are used for this data. The first light map covers the period from October 1, 2011, until February 20, 2012, and the second covers the period from February 20, 2012, until April 15, 2012. Some representative sections of the first light map are shown in Fig. 11.

For a SS event, the correction function is applied by multiplying the sum of the two APD plane signals by $1/f(r,\phi,z)$, while for a MS event, a correction factor is deduced by taking the appropriate charge-cluster energy-weighted sum. The light-map correction function improves the scintillation-only energy resolution at 2615 keV from 7.9% to 6.0% for SS events and from 8.1% to 6.3% for MS events, respectively. The largest correction factor within the fiducial volume is ∼15% (the fiducial cut near the cathode eliminates the region of the detector that sees the largest gradient in the correction function).

2. Electron lifetime correction

Electrons drifting in LXe can be captured on electronegative impurities, leading to an exponential decrease with time. This attenuation is described by

$$N_e(t) = N_0 \exp(-t/\tau_e), \tag{8}$$

where N_0 is the original number of electrons, τ_e is the electron lifetime, and t is the drift time. We correct for this attenuation by measuring the electron lifetime every few days using the ^{228}Th source deployed near the cathode. We divide the data in each TPC into 16 drift-time bins and fit a Gaussian plus error function model to the full-absorption peak in each bin. The central value of the peak is plotted versus drift time as shown in Fig. 12, and the electron lifetime is extracted from a fit to Eq. (8). It is found that the goodness-of-fit function is asymmetric around the minimum and larger electron lifetime values have larger uncertainties.

The electron lifetime varies over time owing to small changes in the xenon recirculation rate, occasional interruptions owing to xenon pump maintenance or failure and power outages, and events where xenon gas is added to the detector

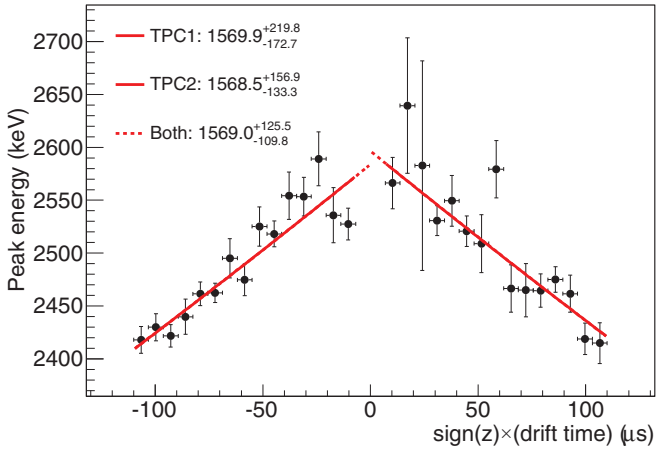

FIG. 12. (Color online) An example electron lifetime τ_e measurement obtained by fitting a decaying exponential to the ^{228}Th full-absorption peak energies binned by drift time. TPC 2 (negative Z) is assigned a negative drift time for convenience in visualization. Fits to separate τ_e for each TPC and the combined fit value are shown. This data are from a single-source calibration run.

by the detector-monitoring system. To account for this, a piecewise polynomial is fit to the measured τ_e history, as shown in Fig. 13. Separate τ_e are used for each TPC to allow for spatial variation in the LXe impurity content, although the two TPCs track each other quite well. A correction factor of $\exp(t/\tau_e)$ is applied to all ionization signals in the data by evaluating the τ_e history function at the time of each event.

3. *Shielding inefficiency corrections*

The shielding inefficiencies of the V grids (see, e.g., Ref. [30]) produce a small residual dependence of the U-wire pulse amplitude on the Z position of the charge deposition. We measure this effect in the data by fitting the purity-corrected peak position of the ^{208}Tl γ line at 2615 keV as a function of Z. We fit these data to the function

$$E_{\text{meas}} = \frac{E_0}{1 + p_0 e^{(|Z| - Z_{\max})/p_1}}, \tag{9}$$

where E_{meas} is the purity-corrected peak energy, E_0 is the true peak energy, Z is the Z coordinate of the energy deposit in units of mm, and $Z_{\max}$ is the maximum drift distance (192.5 mm). We find that the best-fit parameters are $(p_0,\ p_1) = (0.043,$ 7.02 mm) and (0.064, 8.09 mm) for one-wire and two-wire charge deposits, respectively. The function is then inverted to correct the measured charge deposit energy to the true energy. For events in the fiducial region, this correction is much less than 1%.

D. Rotated energy measurement

To optimize the energy resolution of the detector, we take advantage of the microscopic anticorrelation between ionization and scintillation in LXe [21]. This effect is illustrated for ^{228}Th source calibration data in Fig. 14. The optimal energy variable is calculated by combining the charge, E_I, and scintillation, E_S, measurements with appropriate weights

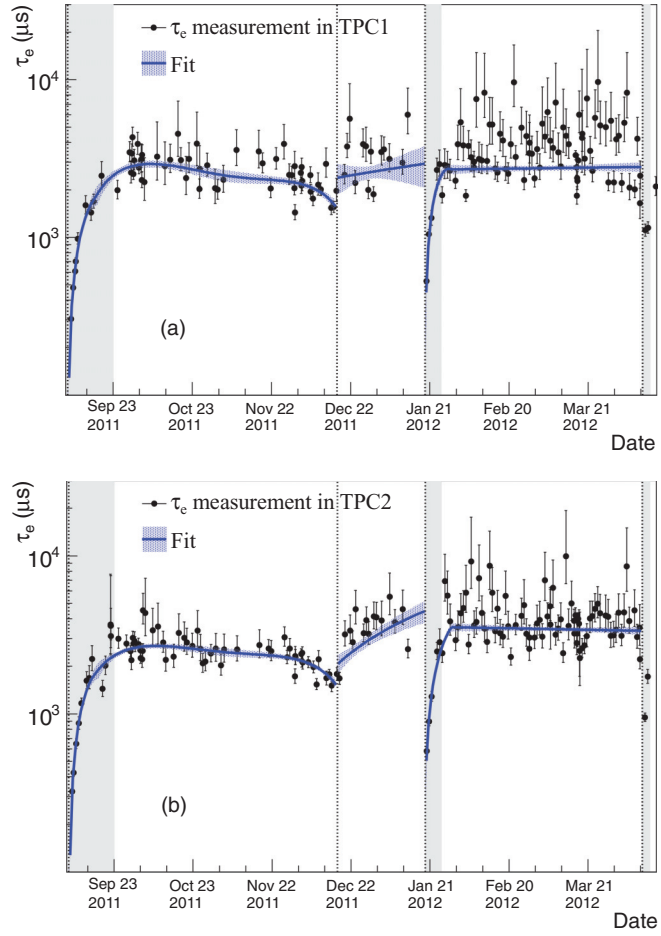

FIG. 13. (Color online) The fit of a piecewise polynomial to electron lifetime in TPC 1 [positive Z (a)] and TPC 2 [negative Z (b)]. The colored bands show the 68% confidence interval on the fit. The vertical dashed lines indicate discontinuities in the electron lifetime owing to interruptions in the xenon recirculation or xenon gas feed events. The vertical shaded regions indicate time periods which were excluded from the final data set owing to poor electron lifetime.

according to

$$E_R = E_S \sin(\theta^R) + E_I \cos(\theta^R), \tag{10}$$

where E_R is the "rotated" energy and θ^R is the rotation angle.

We find that the energy resolution of the ionization channel is nearly constant in time with a value of $\sigma/E = 3.5\%$ and 4% at 2615 keV for SS and MS events, respectively. The scintillation-only energy resolution, however, does show significant time variation, as shown in Fig. 15. The exact cause of this variation is under investigation, but it is likely related to noise in the front-end electronics of the APD channels.

Owing to the variation in the scintillation energy resolution, the optimal θ^R to use in Eq. (10) also varies with time. We measure θ^R weekly with ^{228}Th source calibration data and apply it to calculate the appropriate rotated energy for events in the "low-background data" (physics data) as a function of their date. This is done separately for SS and MS events. We

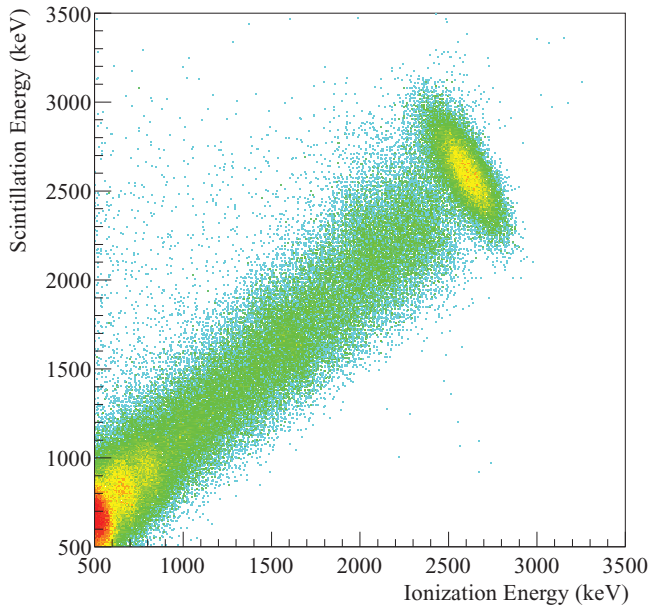

FIG. 14. (Color online) Anticorrelation between ionization and scintillation for SS events from a ^{228}Th source. The prominent island at the upper end of the distribution is the 2615-keV γ line of ^{208}Tl.

apply the same rotation angle to all events regardless of the event energy.

After applying all corrections, the residuals defined as $(E - E_{\text{true}})/E_{\text{true}}$ are 0.36% for ^{137}Cs and 0.17% for ^{60}Co and ^{228}Th sources, as shown in Fig. 16. The energy measured for the ^{40}K peak in the low-background data has a residual of 0.21% and is also shown in Fig. 16.

The energy resolution $\sigma(E)$ is parameterized as a function of energy, $\sigma^2(E) = \sigma_{\text{elec}}^2 + bE + cE^2$, where σ_{elec} is the electronic noise contribution, bE represents statistical fluctuations in the ionization and scintillation, and cE^2 is regarded as a position- and time-dependent broadening. This parametrization is used to smear the Monte Carlo data set to produce the energy PDFs. To estimate the covariance matrix of the resolution parameters, an iterative approach (inspired

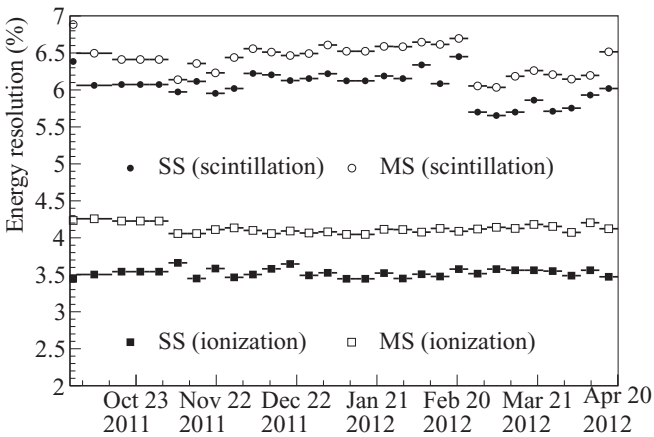

FIG. 15. Energy resolutions of ionization and scintillation channels during Run 2a.

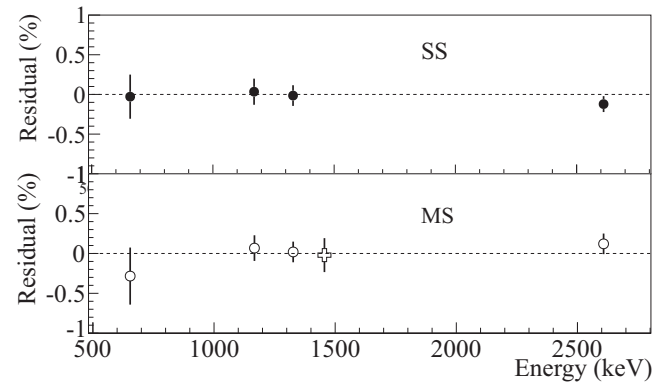

FIG. 16. Residuals between the calibrated source energies and the true energies for SS and MS events. Also shown is the residual for the ^{40}K peak (cross, MS only), which is obtained from the low-background data set.

by Ref. [31]) was developed to fit the smeared ^{228}Th Monte Carlo spectrum to the calibration data set, with an underlying assumption that all the parameters compose a multivariate Gaussian distribution. We calculate the resolution curve $\sigma(E)$ weekly for source agreement studies (see Sec. VI). To take into account the time variation of the energy resolution, the

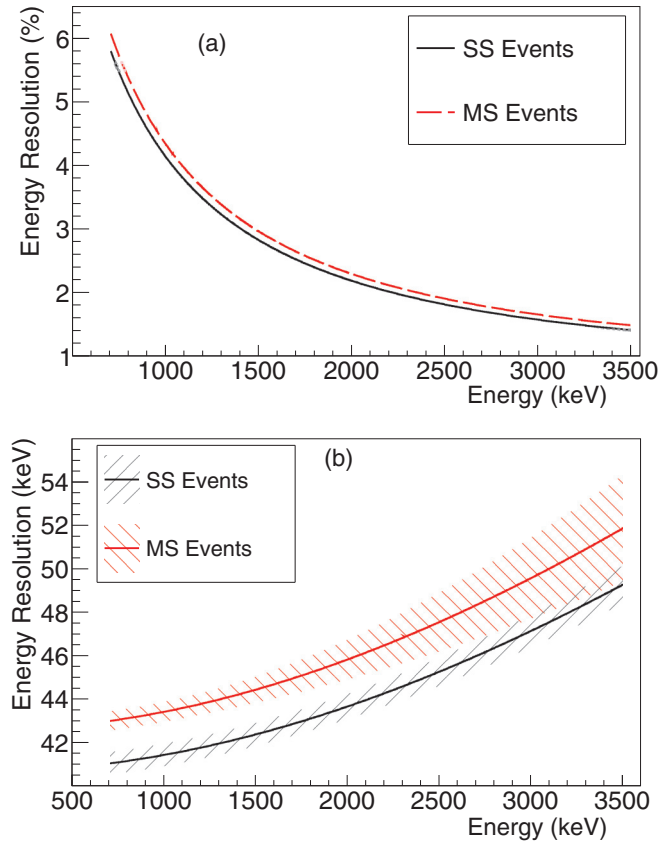

FIG. 17. (Color online) (a) The fractional energy resolution (σ/E) for SS and MS events. The width of the two lines indicates the uncertainty. (b) The absolute energy resolution for SS and MS events. The hatched areas indicate the uncertainty.

^{228}Th Monte Carlo data set is initially smeared by the weekly resolution parameters, then weighted by the low-background live-time fraction in each week. In the end the Monte Carlo ^{228}Th data sets are combined and fitted by using the iterative approach to get the averaged resolution parameters. The time-averaged energy resolution is plotted versus energy in Fig. 17, and its values at the $\beta\beta$ decay Q value are $1.84\% \pm 0.03\%$ ($1.93\% \pm 0.05\%$) SS (MS) events, respectively. These values are slightly different than those reported in Ref. [8] because we now average over time.

VI. MEASUREMENT AND MONTE CARLO SIMULATION AGREEMENT

The maximum-likelihood fit requires, as an input, PDFs in energy and standoff distance space for both the signal and the backgrounds. Separate PDFs, one containing SS events and the other containing MS events, are generated using the EXO-200 simulation package. The energy observable in these simulated PDFs is derived from a convolution of the measured energy resolution function (Sec. V D) and the deposited energy given by the simulation.

An important mechanism for determining the accuracy of simulation-generated PDFs is the direct comparison of the detector response to certified calibration sources with the full detector simulation of the same source. Calibration source data, however, differ from the $2\nu\beta\beta$ signal in several significant ways. The $2\nu\beta\beta$ events are predominantly SS ($\sim$95% SS), whereas the interactions of photons from the external sources are mostly MS ($\sim$20%–50% SS; see, e.g., Fig. 21). In addition, $2\nu\beta\beta$ events occur uniformly throughout the LXe volume while the source of calibration events lies in a single point external to the LXe volume. The photons emitted by the calibration source are strongly attenuated by the LXe, concentrating the interactions in the active xenon nearest to the deployment position of the calibration source.

Because of the differences outlined above, the verification of source agreement is augmented by direct analysis of the low-background data wherever feasible (see Sec. VIII D). The calibration source/simulation agreement studies are partitioned as follows: (A) source shape agreement, which compares the shapes of distributions derived from both; (B) source rate agreement, which considers the ability of the simulation to predict the activity of the source that is observed; and (C) SS fraction agreement, which verifies the fidelity of SS/MS discrimination predicted by the simulation.

A. Source shape agreement

The shape of ^{228}Th and ^{60}Co calibration source energy spectra and standoff distributions were compared to the those from simulation at various calibration source deployment positions. The ^{137}Cs source was not considered because its main feature (the 662-keV γ-ray full-energy absorption peak) lies below the analysis energy threshold (700 keV). The primary source deployment positions near the cathode (S5 and S11) illuminate the bulk of the active LXe in both TPCs. Source calibrations near either anode (S2 and S8) are additionally used to confirm adequate modeling at each end of the TPC.

Figure 18 demonstrates, for the shape of the energy and standoff distance distributions, the agreement between ^{228}Th calibration source (at S5) data and simulation and the agreement between ^{60}Co calibration source (at S2) data and simulation. Figure 19 highlights the Gaussianity of the ^{228}Th and ^{60}Co (at S5) full-energy deposition peaks along with the

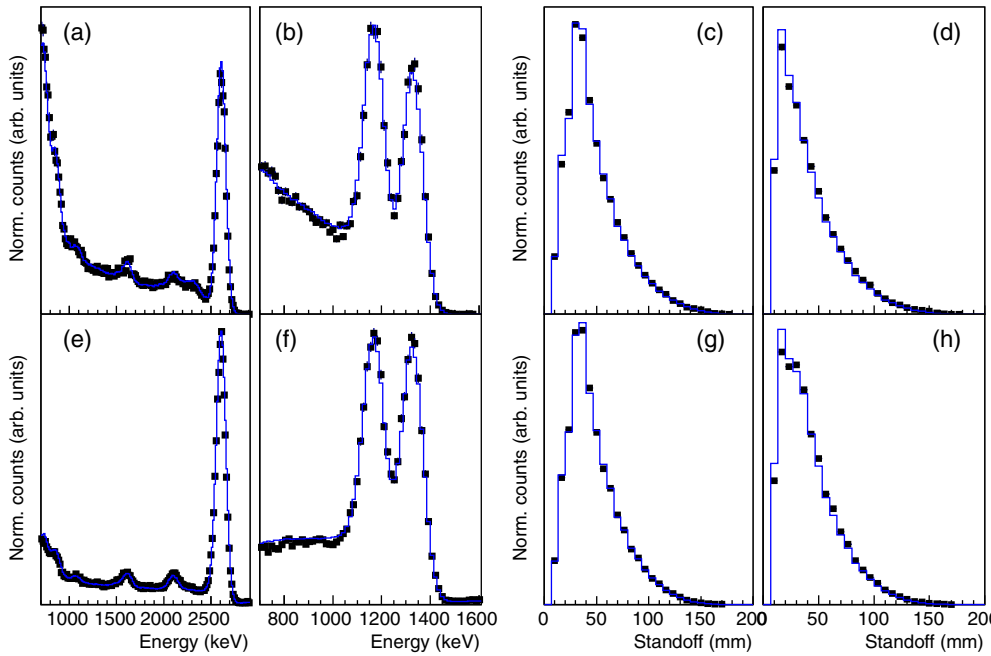

FIG. 18. (Color online) Comparison of shape between data (points) and simulation (histograms) for energy and standoff distance distributions. All distributions have been normalized to 1 and, in all cases, the top (bottom) plots are SS (MS) distributions. Panels (a), (c), (e), and (g) are for a ^{228}Th source near the cathode. Panels (b), (d), (f), and (h) are for a ^{60}Co source located near the anode.

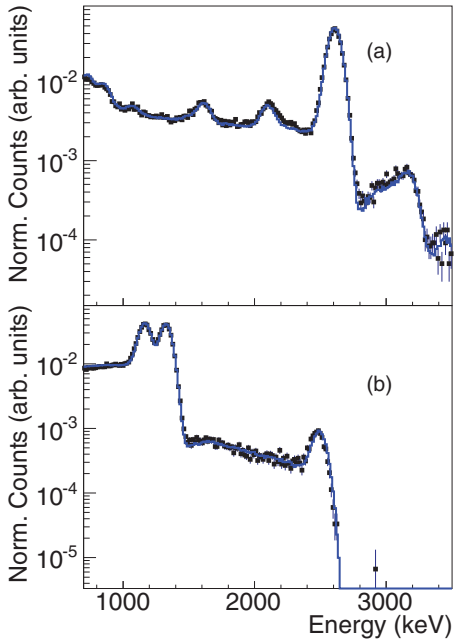

FIG. 19. (Color online) Comparison of MS energy distribution between data (points) and simulation (histograms) using ^{228}Th (a) and ^{60}Co (b) sources near the cathode (S5). Note the excellent agreement of the full-energy-deposition γ-ray peaks all the way up to the summation peaks.

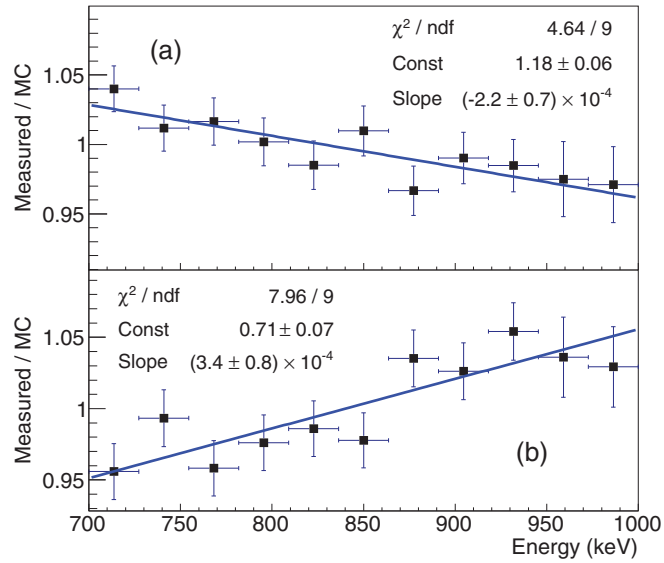

FIG. 20. (Color online) Ratio of ^{60}Co source (at the cathode, S5) calibration spectra to that generated from simulation. Single- and multisite events are shown in (a) and (b), respectively, and linear fits to the data are shown. Ratio plots for ^{228}Th source data and simulation demonstrate the same behavior.

excellent agreement achieved between both sets of calibration data and the simulation in the vicinity of the respective summation peaks. All of these distributions are normalized to unity to study only the shape agreement.

The ratio of ^{60}Co calibration source spectra, below 1000 keV, to that predicted by the simulation is shown in Fig. 20. A linear parameterization as a function of energy is also shown over the data points. Both the ^{60}Co (shown) and the ^{228}Th calibration source data-simulation discrepancies can be parameterized by a single linear function of energy. This suggests a single mechanism is responsible for the common disparate shapes. These linear skewing parametrizations (one for each of the SS and MS energy distributions) are used in Sec. IX C 1 to estimate the systematic error induced in the $2\nu\beta\beta$ rate measurement.

B. Source rate agreement

To test the ability of the simulation to predict the observed activity of the ^{228}Th and ^{60}Co calibration sources, the total number of events passing all selection criteria (see Sec. VIII) was compared between simulation and data. The results from simulations were normalized to the NIST-traceable activity of the respective source and the counting times of the corresponding data sets. The agreement is quantified by the fractional difference [Data − (MC Sim)]/Data in number of events. The results of these studies are listed in Table IV for both calibration sources, deployed at four distinct locations, and indicate that the simulation can predict the activity of external sources within ±4%.

There are several important contributions to this result, which make it not directly reflective of the ability of the simulation to predict the detection efficiency of $2\nu\beta\beta$. In particular, the observed rate of a source depends strongly on its exact position owing to solid angle changes. To quantify how the uncertainty on the source position propagates to the uncertainty on the rate, simulations were generated varying the source locations around their nominal positions. Maximum-likelihood fits between simulation and data were performed using the spatial distributions of events within the TPC at each

TABLE IV. Constraints on the absolute rate agreement at each calibration location, including uncertainties owing to the source location. These numbers, which *do not* include the source activity uncertainty, may be compared to the uncertainty on the absolute activity of the sources, known to be 1.2% from the NIST-traceable certificates issued by the vendor and confirmed through independent collaboration measurements.

Source location	Source type	Absolute rate agreement [Data−(MCSim)]/Data (%)
S2 (anode)	^{228}Th	$3.5^{0.8}_{1.3}$
	^{60}Co	$2.4^{0.4}_{1.6}$
S5 (cathode)	^{228}Th	$1.1^{1.0}_{0.9}$
	^{60}Co	$-3.7^{1.5}_{1.2}$
S8 (anode)	^{228}Th	$-3.2^{0.8}_{0.9}$
	^{60}Co	$1.8^{0.8}_{1.1}$
S11 (cathode)	^{228}Th	$3.1^{2.3}_{2.7}$
	^{60}Co	$1.3^{3.1}_{4.0}$

simulated position. The error in the rates presented in Table IV were taken from the results of these fits.

An additional important consideration is that the simulation predicts fewer MS events to be fully position reconstructed, which would result in the removal of more events in simulation. For external sources of γ rays, of which more than half are observed to be MS, this leads to a more significant underprediction of the activity than would be expected for $2\nu\beta\beta$ decay events, of which only about 5% are observed to be MS. The effect of this underprediction in simulation on the $2\nu\beta\beta$ rate is estimated in Sec. VIII D using low-background data.

C. Single-site fraction agreement

The fraction of SS events, defined as the event number ratio SS/(SS + MS), is calculated from both calibration source data and source simulations. As the SS fraction is observed to be energy dependent, the discrepancy between the SS fraction of calibration source data and the SS fraction of the simulations is determined versus energy. Figure 21 shows that the maximum fractional difference between the SS fraction of calibration source data and the SS fraction of source simulations is ±10%.

From these observations, a spectral-weighted-average SS fraction error is calculated for the $2\nu\beta\beta$ spectrum. This error, determined to be 5.9%, is applied as a constraint in the fit to the low-background data set. Any remaining error on the $2\nu\beta\beta$ rate resulting from the residual energy dependence observed in the SS fraction has been studied using the low-background data and is presented in Sec. IX C 1.

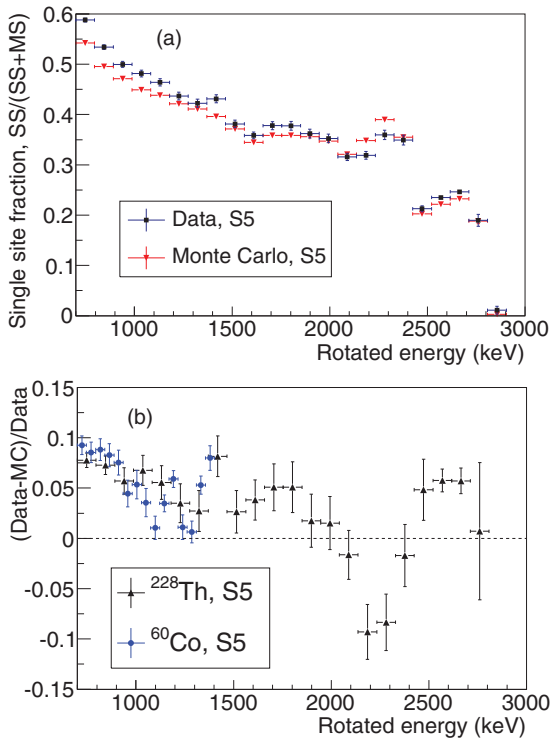

FIG. 21. (Color online) (a) Single-site fraction for ^{228}Th calibration data and simulation. (b) Fractional difference between SS fraction for data and simulation as a function of energy for ^{228}Th and ^{60}Co sources.

VII. DATA QUALITY AND DETECTOR MONITORING

To ensure operational consistency of all relevant detector parameters over the data-taking period, a number of environmental and analytic parameters are monitored. This monitoring enables a quantitative assessment of the quality of data taken within a particular time period, which we use when selecting runs for the physics analysis. Checks include muon veto system monitoring, low-level checks, and high-level checks, the last of which requires data to be processed with the analysis framework described in Secs. II C and IV. Observations made by monitoring shifters during the run are additionally taken into account to ensure that external activities not monitored by the DAQ system (e.g., construction or mine activity) do not have an adverse affect on the data. The runs selected for the physics analysis total 135.2 days, representing ∼77% of the total low-background data taken during Run 2a (23% loss owing to data quality requirements).

A. Muon veto system source campaigns

The health and response of the muon veto system is evaluated twice per year with a ^{60}Co source and a stand-alone DAQ system employing a charge-sensitive ADC. This monitoring program is necessary owing to the large environmental temperature swings to which the system is exposed outside of the EXO-200 clean rooms. This may lead to yellowing of the scintillator, PMT failure, or cracks in the PMT optical coupling. During these campaigns the ^{60}Co source is placed at four different distances to each instrumented end of each of the 29 veto panels. The average signal from of backscattered ^{60}Co γ's is determined by fitting the Compton edge, $p(x_j,t_i)$, in the spectral distributions of each instrumented detector end, where t_i denotes the time of the measurement and x_j the distance of the source from the PMTs. i identifies the calibration campaign; j numbers the different distances. It is assumed that the scintillator light yield L is time and location independent. This gives an expression for the Compton edge,

$$p(x_j,t_i) = g(t_i)Le^{-x_j/\lambda(t_i)},$$

where $g(t_i)$ denotes the time-dependent product of PMT gain and quantum efficiency and $\lambda(t_i)$ is the light attenuation length. Forming two ratios of the measured Compton edges allows both detector parameters to be tracked independently:

$$\frac{p(x_j,t_i)}{p(x_1,t_i)} = e^{-(x_j-x_1)/\lambda(t_i)}. \quad (11)$$

A fit to the distance dependence of Compton edge ratios (normalized to one at the closest distance to the PMTs in a particular calibration campaign), as shown in Eq. (11), determines the light attenuation length of each panel at time t_i,

$$\frac{g(t_i)}{g(t_2)} = \frac{p(x_1,t_i)}{p(x_1,t_2)}e^{x_1[\lambda(t_2)-\lambda(t_i)]/[\lambda(t_2)\lambda(t_i)]}. \quad (12)$$

Knowledge of attenuation lengths at time t_i and for the reference measurement at time t_2 allows the computation of the relative gain change of the PMTs from the ratio of Compton edges given in Eq. (12). The ratio is corrected for the change in light attenuation length. The second calibration campaign

serves as the reference data set as threshold settings were not finalized during the first calibration.

The attenuation length and gain-ratio data exhibit linear trends for all panels. The data indicate an average rate of change per year of $\Delta\lambda/\lambda_2 = -2.9\%$ with an rms of 5.9% and $\Delta g/g_2 = -5.2\%$ with an rms of 8.5%, showing adequate stability in the system's response to ionizing radiation.

B. Low-level checks

A typical low-background run has a duration of ∼24 h, although, occasionally, shorter runs are taken. A number of baseline requirements must be met for a low-background run to be used in the physics analysis:

(1) run length greater than 1800 s;
(2) average solicited trigger rate measured within 0.5% of its nominal value (0.1 Hz);
(3) calculated live time no more than 30 s different than the run duration.

The run-length requirement ensures enough statistics for the calculation of data quality indicators. The second and third requirements ensure that the DAQ system is operating nominally throughout the run and that no significant reductions in live time caused by noise bursts or DAQ interruptions have been seen.

C. High-level checks

The higher level checks involve monitoring the following:

(1) the electron lifetime τ_e;
(2) the efficiency of muon veto system;
(3) rates of certain classes of events.

Runs satisfying all checks may be automatically approved to be used in the physics analysis. Those runs that do not satisfy all checks are not immediately rejected, but are instead subjected to additional scrutiny to determine their final status.

1. Electron lifetime

Even though the charge data are corrected for the effects of finite electronegative purity, as described in Sec. V C 2, uncertainty in the electron lifetime correction or rapid changes in the purity can degrade the detector energy resolution. We calculate that this contribution is acceptably small when the electron lifetime is greater than 1 ms. We also calculate that for an electron lifetime of 1 ms, a rate of change of 500 μs/day can contribute 1.04% to the energy resolution. Hence, the following requirements on the detector purity are applied:

(1) $\tau_e > 1000$ μs;
(2) four or more consecutive measurements of similar electron lifetimes over several days with constant xenon recirculation (this ensures stability of the purity);
(3) that τ_e not be increasing at a rate >50% or decreasing at a rate >25% of the previous measurement per day.

The variation of the electron lifetime during Run 2a is shown in Fig. 13.

2. Muon veto panels

The absolute efficiency of the individual veto panels is monitored biannually as described in Sec. VII A. The muon veto system is also monitored semicontinuously with low-background data by counting the fraction of events identified as muons in the TPC that are also tagged with a veto trigger within 2 μs. For the Run 2a data set this fraction is 0.9618 ± 0.0021 on average.

The individual veto panels are monitored on a run-by-run basis as follows. Because of geometrical effects, the TPC-correlated muon rate varies among veto panels. If one or more panels do not register a single trigger during a low-background run, and those panels account for more than 5% of the average veto-TPC coincidence rate, then the run is rejected. This threshold was chosen so that the global veto system efficiency remains >90%, which is a requirement for achieving the background goals of the $0\nu\beta\beta$ search.

3. Event rates

Rates of different classes of events are monitored over time, as deviations from mean rates can provide an indication of a detector problem or an important environmental change. In particular, rates of the following seven classes of events are monitored, with rough, nominal rates of each class given parenthetically: (a) events tagged as noise by the analysis processing (10 mHz); (b) reconstructable events, defined as having at least one scintillation cluster and not tagged as a muon, noise, or a solicited trigger (35 mHz); (c) nonreconstructable events, those failing criteria (b) and not tagged as a muon, noise, or a solicited trigger (25 mHz); (d) events with >0 keV (25 mHz); (e) events with >300 keV (20 mHz); (f) events with >1000 keV (3 mHz); and (g) events with >2000 keV (1.5 mHz). The energy ranges in the last four classes of events are defined for ionization energy. For each of these seven rates, an acceptance region is defined so that a value falling within these limits confirms the data as high quality. An example set of plots is given for event classes (a) and (b) in Figs. 22 and 23, respectively, showing the rate versus time as well as the distribution of rates of the two parameters over the data-taking period.

VIII. EVENT SELECTION REQUIREMENTS

The live time of the data set differs from the data-taking time owing to the following rejection criteria, with the percentage live time lost owing to each in parentheses:

(1) 1 ms before to 25 ms after the muon veto system triggers (0.6%);
(2) 1 μs before to 60 s after TPC events tagged as muons (4.5%);
(3) portions of runs flagged as coincident with poor data-taking conditions, including times during a run where one or more of the selection criteria described in Sec. VII are not satisfied (0.6%);
(4) 60 s after the beginning and 1 s before the end of any run (<0.1%).

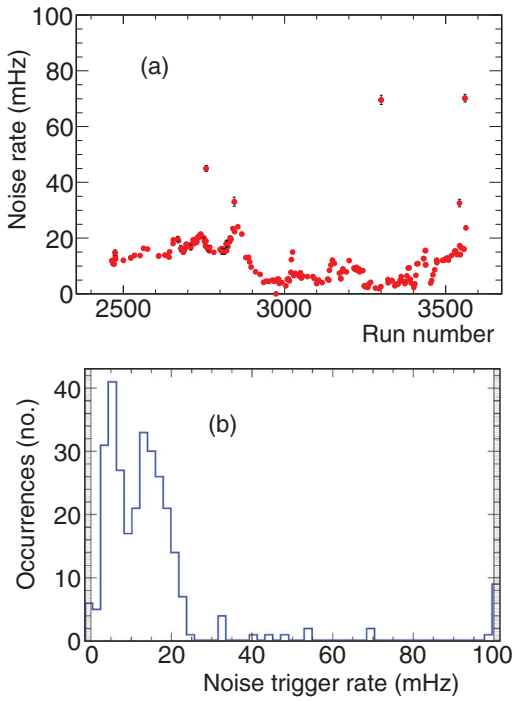

FIG. 22. (Color online) History (a) and distribution (b) of rate of events tagged as noise. The drop in noise starting with run 2855 is attributable to a cooling fan change in the electronics box. The unshaded region in (b) indicates the accepted parameter values ranges.

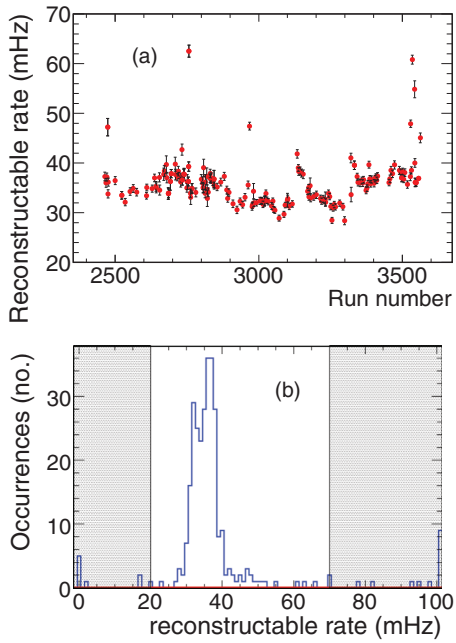

FIG. 23. (Color online) History (a) and distribution (b) of the rate of events that have at least a scintillation and charge cluster. The increase in rate seen after January 13, 2013 (run 3121), came from increased Rn in the system after a Xe feed event. The discontinuity on February 22, 2013 (run 3333), was from an APD electronics change. The unshaded region in (b) indicates the accepted parameter values.

These result in a total live-time reduction of 5.6% over the total data-taking time of all selected runs in the Run 2a data set. This does not exactly correspond to the sum of the above percentages because some of the criteria overlap.

Selection criterion (1) is motivated by the observed elevated event rate in the TPC following a muon veto system trigger. This rate is found to return to its nominal value after 25 ms. In addition, the analysis of the time behavior of 2.2-MeV full-energy deposition events within 25 ms following a muon trigger yields a neutron capture time in hydrogen in the HFE of 740 ± 120 μs, well within the 25-ms time window. Selection requirement (2) is motivated by the expectation of the cosmogenic activation of short-lived isotopes in and near the LXe following a muon event in the TPC. The 60-s coincidence window is determined by limiting the impact of this requirement on the live time of the data set to be $<5\%$.

Data-taking times may be flagged as unacceptable [criterion (3)] owing to data quality concerns arising from, e.g., bursts of electronic noise or mining activity. Criterion (4) ensures that neither a muon TPC event or an event within 1 s coincidence could have been missed immediately before the initiation of or immediately after the termination of a run. The application of these live-time selection criteria results in $127.6^{0.012}_{0.000}$ days live time out of 135.2 days of cumulative data taking during all selected runs in the Run 2a data set.

The following data-selection criteria are evaluated on an event-by-event basis. For each data reduction, the resulting loss of $2\nu\beta\beta$ signal efficiency is estimated along with an associated error. These efficiencies are used to correct the measured $2\nu\beta\beta$ and the associated errors in the $2\nu\beta\beta$ rate are included via a normalization term (see Sec. IX B). The following data reductions are applied in the order that they are listed (note that event frames are 2048 μs in length). For events to be selected for analysis they must

(1) not be in coincidence with 0.1 Hz solicited triggers (explicitly tagged by the DAQ system);
(2) not be in coincidence with events tagged as noise;
(3) not occur within 1 s of another TPC event [to address, e.g., bismuth-polonium (Bi-Po) fast β-α coincidences in the ^{222}Rn and ^{220}Rn decay chains and other correlated decays];
(4) not contain more than one reconstructed scintillation signal;
(5) not begin within 120 μs of the end of the waveform trace;
(6) not contain any partially reconstructed signals (must be fully 3D reconstructed);
(7) be reconstructed inside the fiducial volume;
(8) not exhibit a high light-to-charge ratio (e.g., appear to be α-like);
(9) contain total rotated energy >700 keV.

The estimation of systematic errors related to items (3)–(7) are described in more detail in the following sections. The removal of solicited triggers results in a $10^{-3}\%$ reduction of signal efficiency, estimated from the probability of a solicited trigger occurring coincidentally with a $2\nu\beta\beta$ event. A comparable reduction in signal efficiency ($10^{-3}\%$) has been

calculated for events tagged as noise. Whereas the majority of noise events are tagged because of grossly unphysical characteristics (e.g., channel range saturation), there is a possibility that some physics events are falsely tagged as a particular class of noise. The probability of this occurring has been estimated by randomly selecting a set of events failing this cut and hand scanning them. No false positives were found, leading to a conservative $6 \times 10^{-2}\%$ systematic error on the signal efficiency.

Events with a high light-to-charge ratio are indicative of an event including α particles or of events with incomplete charge collection, which may occur if the charge cloud drifts to the edges of the wire grid. This cut is highly degenerate with some of the other selection cuts and, after the previous application of all other cuts, only removes ∼35 events from the 23 082-event data set. We conservatively take this ratio (0.15%) as a systematic error.

The removal of events below the threshold of 700 keV is subject to errors in the measurement of the detector calibration and resolution. The contribution of this effect to the $2\nu\beta\beta$ measurement was found to be 0.4%, estimated by the residual calibration error of the ^{137}Cs 662-keV peak (see Sec. V D).

A. Scintillation-signal-driven data selection

Two cuts are performed, which are related exclusively to scintillation signals. Events which have a scintillation signal within 120 μs of the end of a waveform are removed because they cannot be fully reconstructed. This cut removes only one event from the final data set, therefore contributing a negligible amount to the systematic error on the efficiency.

In addition, events are required to have no more than one scintillation signal to remove correlated decays (e.g., Bi-Po correlated decays). The false-positive rate (the probability to incorrectly reconstruct more than one scintillation signal when only one *real* signal exists) has been estimated by running the reconstruction software on noise trace (solicited trigger) events from data with an added simulated signal of known amplitude. This study estimates a false-positive rate integrated above 700 keV of <0.1%. This study was cross checked by analyzing the 613 low-background events removed by this cut after applying all other analysis cuts and was determined to remove 0.7% of all events because of an incorrectly found scintillation signal. We choose to take the more conservative value and so a normalization error of 0.7% is added to account for this effect.

B. 1-s event-to-event coincidence

A 1-s coincidence cut on TPC events is used to reduce the presence of backgrounds arising from fast, correlated decays in the TPC that may arise, for example, after through-going muons or from the decays of radioactive species in the LXe (Bi-Po decays) not removed by the scintillation event cut. For the purpose of this cut, two TPC events are considered to be in coincidence if their DAQ triggers were not solicited, the events are not tagged as correlated noise, and both events have some scintillation signal or saturate a scintillation channel. The $2\nu\beta\beta$ signal efficiency was calculated by considering the rate of random coincidences of TPC events and was determined to be 0.931 ± 0.002.

C. Fiducial volume selection

The fiducial volume is chosen to include regions of the detector that are well understood and properly modeled in simulation. Because the measurement of the $2\nu\beta\beta$ half-life is not constrained by statistics, a smaller fiducial volume is chosen than was presented in Ref. [8] to minimize the impact of fiducial-volume-related systematics on the result. As in Ref. [8], because signals are fundamentally reconstructed at U and V coordinates parallel to the detector wire channels, the fiducial volume is chosen to be hexagonal in shape, thus avoiding effects arising from radial coordinate transformations. However, this still requires using a third coordinate (X) derived from U and V to define the hexagon. This is because the U- and V-coordinate axes are each perpendicular to two sides of the hexagon, whereas the last two sides are perpendicular to the derived X axis (see Fig. 2).

The Z range of the fiducial cut is chosen to include events satisfying 182 mm $> |Z| >$ 15 mm in both TPC halves, or 10.2 mm from the V-wire planes and 15 mm from the cathode. The distance from the V-wire plane ensures the grid efficiency correction to the charge energy (see Sec. V C 3) is $\ll$1%. The distance from the cathode was determined from studies using the 3D electric field model (see Sec. III B), which demonstrated slightly distorted (not parallel in Z) charge drift trajectories within 15 mm of the cathode.

To determine the cut in the U- and V-coordinate system, the SS $2\nu\beta\beta$ rate was studied as a function of detector position by fitting the low-background spectrum in separate hexagonal position bins. The results of this study are shown in Fig. 24. We choose the apothem of the hexagonal fiducial volume to be 153 mm, as indicated in Fig. 24 and illustrated in Fig. 2. This cut removes events on the boundaries of the sensitive area of the hexagonal wire plane. The rate of $2\nu\beta\beta$ decay was also studied in Z position bins and found to be independent of position within the chosen fiducial volume. The fiducial volume selected in this way corresponds to 27.08 L of liquid Xe, corresponding to 66.20 kg of ^{136}Xe. See Sec. IX C 5 for a discussion on the error on this number.

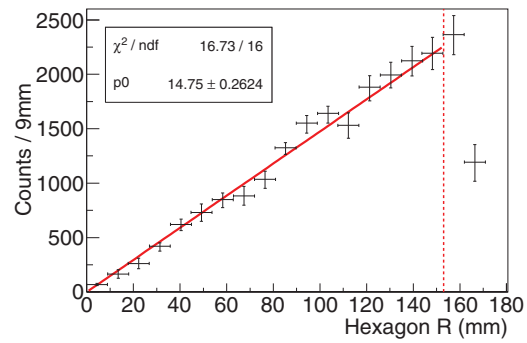

FIG. 24. (Color online) Rate of $2\nu\beta\beta$ versus hexagonal apothem. The vertical dashed line indicates the fiducial cut we have chosen to use at an apothem of 153 mm. The data within that region are consistent with a rate that is proportional to volume.

To understand the error on the chosen fiducial volume we first study the cluster position reconstruction accuracy in the two original coordinates: U, V. Given that the detector has a discrete wire spacing, the position resolution is finite and the expected uncertainty is given by the standard deviation of the uniform distribution. For a 9-mm wire pitch in the U and V directions this gives ± 2.6 mm for uniformly distributed events.

To study the position reconstruction uncertainty in simulation we generate the distribution of differences between reconstructed cluster coordinates and true location of simulated charge deposits of a $2\nu\beta\beta$ source. The average rms is 1.2 mm in the V direction and 2.4 mm in the U direction, and both distributions are centered on zero with negligible bias. The small rms in the V direction arises owing to the larger number of multiwire events, which allow better position determination through weighted averaging. The third coordinate that defines the hexagonal volume, X, is different than the fundamental coordinates U and V because it is a combination of the two and so may be subject to an additional uncertainty owing to errors in the clustering algorithm (e.g., incorrect wire association). The uncertainty on the X coordinate was determined to be 2.6 mm, consistent with the individual U and V errors added in quadrature, indicating that the clustering error is negligible.

We can cross check these numbers with the data for specific cases, in particular by using α and β decays from the cathode that deposit energy in both TPC halves. Such events typically originate from a common position on the cathode and can be used to check how accurately both TPCs reconstruct a shared coordinate. Because the U (V) wires in TPC1 are parallel to the V (U) wires in TPC2, these events may be used to cross-check the U and V position reconstruction. The distributions of $U_{\mathrm{TPC1}} - V_{\mathrm{TPC2}}$ and $V_{\mathrm{TPC1}} - U_{\mathrm{TPC2}}$ both have a width of 3.07 mm, consistent with the uncertainties obtained in the Monte Carlo simulation study considering that the measurement of $U - V$ corresponds to a measurement of the sum of ΔU and ΔV. The mean values are 0.4 mm for $U_{\mathrm{TPC1}} - V_{\mathrm{TPC2}}$ and 1.5 mm for $V_{\mathrm{TPC1}} - U_{\mathrm{TPC2}}$, which could be explained if the wire planes do not exactly mirror one another. Because we do not have an independent measurement of the wire-plane alignment after cooling the TPC with sufficient precision to confirm this possibility, a systematic uncertainty of 1.5 mm on the reconstructed U and V positions is included in the overall fiducial volume uncertainty to account for any residual bias.

The overall error on the reconstructed Z position for events drifting the full length of each TPC can be determined from the drift-time distributions for α particles emitted from Rn-daughter contamination on the cathode, as shown in Fig. 25. The observed drift-time distributions for α events originating on the cathode have means of 115.224 ± 0.006 μs and 115.891 ± 0.006 μs for TPC1 and TPC2, respectively. The widths of the drift-time distributions, $\sigma_{t,\mathrm{TPC1}} = 0.411 \pm 0.006$ μs and $\sigma_{t,\mathrm{TPC2}} = 0.421 \pm 0.005$ μs, correspond to the expected error on the determination of Z for a single cluster for a given charge drift velocity. Assuming the same drift velocity in both TPCs and using the expected spacing between the wire planes gives an error in Z of $\sigma_Z = 0.42$ mm for an individual cluster. The 0.6-μs difference in the means between

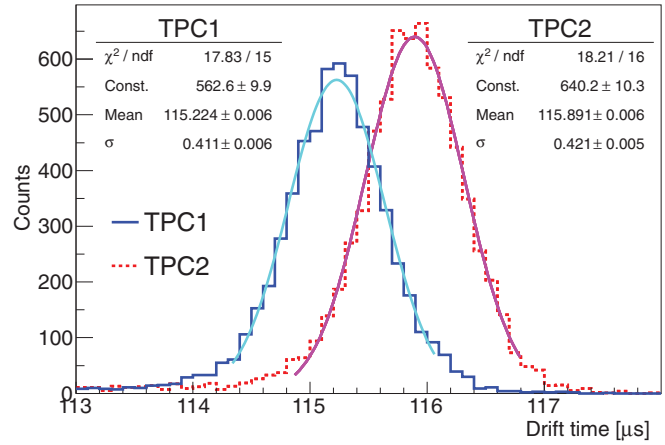

FIG. 25. (Color online) Drift-time distribution for α events originating from the cathode for events collected in TPC1 (solid histogram) and TPC2 (dashed histogram). Gaussian fits to the distributions and their results are also shown.

the TPC halves was verified using an independent analysis that determined the maximum drift time for the distribution of events observed in ^{228}Th calibration data with the source positioned at the cathode. This offset may be accounted for if the cathode were offset by 0.5 mm from center in the direction of TPC1, which is within the expected tolerance after vessel cool down. As with the observed U, V position bias, this offset is included as a systematic error on the Z position to account for the possibility that this bias instead arises from an error in the position reconstruction.

The respective errors on the component coordinate reconstruction are propagated to the fiducial volume error, including any possible biases introduced by the cut. A 0.42-mm spread in the Z direction would only result in a systematic bias on the chosen volume if the cut position was in the region where the density of reconstructed events is different inside and outside the cut (e.g., if the cut was close to the cathode or wire planes). As this is not the case for the chosen Z cut location, there is no systematic bias in the number of selected events.

In the case of the U, V, and X directions, varying the fiducial cut by 1σ above (below) the default cut position does *not* result in the addition (subtraction) of an equal amount of volume. This means that for a constant density of events the cut will be biased to accept *more* events. We estimate this effect to be $+0.36\%$ by varying the fiducial cut and comparing the selected number of events in the hexagonal layer 1σ above and below the default cut position.

The uncertainty on the Z position of the cathode translates to the $\pm 0.3\%$ systematic error on the selected volume, given the cut position. The 1.5-mm uncertainty in U and V positions corresponds to $\pm 1.7\%$ error on the chosen volume. Combining the uncertainty in the Z and U/V directions in quadrature, the total error on the chosen fiducial volume is $\pm 1.73\%$. We choose to add the above bias of $+0.36\%$ symmetrically (i.e., $\pm 0.36\%$) in quadrature with $\pm 1.73\%$, which yields a total systematic error on the normalization owing to the fiducial volume cut of 1.77%.

TABLE V. Signal efficiency and associated systematic errors for events occurring in the fiducial volume and above threshold introduced by event selection requirements. Signal efficiency reductions are corrected for in the final $2\nu\beta\beta$ measurement. Listed errors contribute directly to the final systematic error on the $2\nu\beta\beta$ measurement.

Cut type	Signal efficiency (%)	Error (%)
Solicited triggers	99.99	–
Noise	100	<0.06
1 s coincidence	93.1	0.2
>1 scintillation signal	100	$^{0.7}_{0.0}$
Partial reconstruction	93.9	1.6
Fiducial volume	–	1.77
Light-to-charge ratio	100	0.15
Energy >700 keV	–	0.4
Total	87.4	2.53

D. Rejection of partially reconstructed events

The requirement that all events are fully reconstructed ensures that the fiducial volume cut and position-dependent corrections (see Sec. V C) have been properly applied. The Monte Carlo simulation is used to calculate the efficiency of this cut, which is defined as how often, given an event of a certain energy, all clusters in the event have reconstructed U, V, and Z positions. We estimate the resultant systematic error on the $2\nu\beta\beta$ measurement by looking at the discrepancy between the simulation model and data. As noted in Sec. VI B, the simulation models fewer events with full position reconstruction in the MS spectra for external sources than observed in data. To estimate the systematic difference between simulation and data for the $2\nu\beta\beta$ signal, the result of the fit to the low-background data is taken and background subtracted to obtain a more pure $2\nu\beta\beta$ sample. This is done both before and after applying the partial reconstruction cut, and the "efficiency" is calculated, defined as the integrated event count above 700 keV of the spectrum *with* the cut applied, divided by the number of events *without* the cut applied. This value [93.9 ± 0.2 (stat)%] can be compared directly to the value calculated for simulation for the $2\nu\beta\beta$ PDF (94.2%). There are two primary sources of error that come from using this background subtraction method: uncertainty from the background normalizations and the systematic discrepancy (4%) seen between simulation and data for this cut for external γ sources. The propagation of these errors was performed by generating a toy Monte Carlo data set, drawing the normalization of the different background components from the correlation matrix measured from the low-background fit. The 4% systematic difference observed for source data was incorporated as a corresponding error on the cut efficiency calculated for each background component. The systematic error on the $2\nu\beta\beta$ result is then taken from the 1σ width of the efficiency distribution, which translates to a 1.6% error.

Table V provides a summary of the efficiency reduction and associated systematic errors introduced by the event selection cuts presented in this section.

IX. FIT TO THE LOW-BACKGROUND DATA

A. Fit model

To derive the number of $2\nu\beta\beta$ events from the Run 2a data set, we fit both single- and multisite event sets with their corresponding probability density functions using a binned maximum-likelihood method. The data are binned in energy (200 bins, $700 < E < 3500$ keV) and standoff distance (SD) (20 bins, $0 < r_{\rm SD} < 200$ mm) and the negative log-likelihood function is defined as

$$-\ln L = \sum_i \left[\left(\mu_i^{\rm SS} + \mu_i^{\rm MS}\right) - \left(k_{{\rm obs},i}^{\rm SS} \ln \mu_i^{\rm SS} + k_{{\rm obs},i}^{\rm MS} \ln \mu_i^{\rm MS}\right)\right] + G_{\rm const}, \tag{13}$$

where $k_{{\rm obs},i}^{\rm SS(MS)}$ are the number of SS (MS) counts observed in a given bin i, $\mu_i^{\rm SS(MS)}$ defines the expected number of SS (MS) events from the fit model in the ith bin, and the sum proceeds over all 4000 bins in energy and SD space. $G_{\rm const}$ are Gaussian constraints applied to the fit, which are described in more detail in Sec. IX B. μ_i may be written as

$$\mu_i^{\rm SS(MS)}(\boldsymbol{s},\boldsymbol{n},N) = \int_{i^{\rm th}\,{\rm bin}} F^{\rm SS(MS)}(\boldsymbol{s},\boldsymbol{n},N,\boldsymbol{y})\,d\boldsymbol{y}, \tag{14}$$

which is a function of SS/(SS+MS) fractions for each PDF, $\boldsymbol{s}$, the relative number of events in different PDFs, $\boldsymbol{n}$, and an overall normalization parameter, N, used to include the error on detector efficiency (see Sec. IX B). The integral is performed over the ith bin for the observables energy and SD [$\boldsymbol{y} = (E, r_{\rm SD})$]. $F^{\rm SS(MS)}$ are defined as

$$F^{\rm SS}(\boldsymbol{s},\boldsymbol{n},N,\boldsymbol{y}) = N \sum_j n_j s_j f_j^{\rm SS}(\boldsymbol{y}), \tag{15}$$

$$F^{\rm MS}(\boldsymbol{s},\boldsymbol{n},N,\boldsymbol{y}) = N \sum_j n_j (1-s_j) f_j^{\rm MS}(\boldsymbol{y}), \tag{16}$$

where the sums are performed across the total number of PDFs included in the fit ($N_{\rm PDF}$), s_j is the relative fraction of SS events in PDF j ($\boldsymbol{s} = \{s_0, \ldots, s_{N_{\rm PDF}}\}$), n_j is the total number of events in PDF j ($\boldsymbol{n} = \{n_0, \ldots, n_{N_{\rm PDF}}\}$), and $f_j^{\rm SS(MS)}(\boldsymbol{y})$ is the jth PDF for SS (MS) events and a function of energy and SD.

The list of components comprising the total model is $2\nu\beta\beta$, $0\nu\beta\beta$, backgrounds in the copper vessel (^{238}U, ^{232}Th, ^{40}K, ^{60}Co, ^{65}Zn, and ^{54}Mn), backgrounds in the liquid Xe (^{135}Xe and ^{222}Rn), and backgrounds in the air gap between cryostat and lead wall (^{222}Rn). The PDFs for the background isotopes were produced using the standard GEANT4 radioactive decay module (RDM) generator [22]. For ^{232}Th and ^{238}U the entire chains of decays, assumed in secular equilibrium, are used. For ^{222}Rn, only decays between ^{222}Rn and ^{210}Pb are used. The $2\nu\beta\beta$ event generator uses the Fermi function suggested in Ref. [32].

Additional sources of radioactive background were also considered to be added to the background model, in particular ^{238}U and ^{232}Th in the surrounding HFE fluid. However, studies comparing the shapes of these backgrounds in both the energy and the SD distributions found no significant differences with the corresponding distributions from simulated backgrounds in the copper vessel and so these additional PDFs were not

included in the background model of the fit. This implies that values returned from the fit (e.g., $n_{\mathrm{Th-232,copper}}$) also include contributions from backgrounds located further away from the detector.

B. Constraints

Using the results of additional studies, several Gaussian constraints are added to the negative log-likelihood function [G_{const} in Eq. (13)]. In particular, these constraints contribute a function to [Eq. (13)],

$$G_{\mathrm{const}}(\boldsymbol{\rho},\boldsymbol{\rho_0},\boldsymbol{\Sigma}) = 0.5(\boldsymbol{\rho}-\boldsymbol{\rho_0})^T\boldsymbol{\Sigma}^{-1}(\boldsymbol{\rho}-\boldsymbol{\rho_0}), \tag{17}$$

where $\boldsymbol{\rho}$ is the vector of constrained parameters, $\boldsymbol{\rho}_0$ is the set of expectation values for each parameter, and $\boldsymbol{\Sigma}$ is the covariance matrix for the set of parameters. For each uncorrelated parameter, ρ_i in $\boldsymbol{\rho}$, Eq. (17) contributes the term

$$0.5\left(\frac{\rho_i-\rho_{i,0}}{\sigma_i}\right)^2 \tag{18}$$

to Eq. (13), where $\rho_{i,0}$ (σ_i) is the expected value (error) of ρ_i. The constraints in the fit are as follows.

(i) ^{222}Rn decays are monitored as a function of time and found to occur at a rate of 3.65 ± 0.37 μBq/kg in the xenon. This number is used to constrain the following background contributions:

(1) Rn in the active xenon,
(2) ^{214}Bi on the cathode, and
(3) Rn in the inactive xenon.

^{222}Rn and its daughters decay in the bulk xenon, creating positive ions which drift toward the cathode. This causes a large fraction of the ^{214}Bi decays to occur on the surface of the cathode [item (2)] rather than in the bulk [items (1) and (3)]. Studies of ^{214}Bi to ^{214}Po coincidences in the LXe have shown this drift and demonstrated that 83% of these coincidences occur on the cathode, with the remaining 17% in the bulk. There is $\sim$30 kg of inactive xenon, yielding a total activity of $\sim$110 μBq in this part of the detector. The total activity is divided correspondingly between the three types of simulated events, translated into number of events and is used as a correlated constraint during the fit. This correlation is relaxed to 90% to account for the estimated systematic error (10%) on the calculated relative fractions of items (1)–(3).

(ii) The SS fractions of all components (s) are independently constrained using the 5.9% error determined in Sec. VI C. This means that for each PDF the term $0.5([s_i - s_{i,0}]/[0.059 s_{i,0}])^2$ is added to Eq. (13), where $s_{i,0}$ is the SS fraction given for the ith PDF by the Monte Carlo simulation.

(iii) The overall normalization, N, is allowed to float within constraints determined by the total externally estimated systematic errors in Sec. IX C. This adds the term $0.5([N-1]/0.0260)^2$ to Eq. (13).

C. Summary of systematic errors

In addition to the systematic errors arising from event-selection cuts described in Sec. VIII, several additional components contribute systematic errors on the measured number of $2\nu\beta\beta$ decays.

1. Simulation model inadequacies

As noted in Sec. VI A, there is an energy-dependent discrepancy seen between measured and simulated energy distributions of ^{228}Th and ^{60}Co sources. This discrepancy was used to produce linear skewing functions, an example of which is shown in Fig. 20. To estimate the general effect of simulation model inadequacies on the $2\nu\beta\beta$ measurement, similar linear skewing functions were also produced for the $2\nu\beta\beta$ PDF by comparing the $2\nu\beta\beta$ model generated from simulation with the background-subtracted low-background spectra produced in Sec. VIII D.

The skewing functions were then used to distort the PDFs in the fit model: The functions generated for $2\nu\beta\beta$ were used for "β" -like PDFs ($2\nu\beta\beta$, $0\nu\beta\beta$, and ^{135}Xe) and the functions for sources generated in Sec. VI A were used for the remaining PDFs. These PDFs were used to produce $\sim$1000 toy Monte Carlo data sets by using the expected counts for each PDF given by the low-background fit results. These toy Monte Carlo data sets were fit with the default, "unskewed" PDFs, and the best-fit $2\nu\beta\beta$ value compared with the true value. With this study, it was found that the best-fit $2\nu\beta\beta$ value could be biased -0.33% with respect to the true value. A systematic error on the $2\nu\beta\beta$ measurement of $\pm 0.33\%$ is added to account for this bias, without applying any correction.

2. DAQ related

While performing data quality control for Run 2a, it was determined that during a portion of the run time (5.2% of the live time), a single U-wire channel was not being read out. Studies were performed to determine the effect on the signal efficiency by comparing the default simulated-generated PDFs with modified PDFs. These modified PDFs were the combination of the default PDFs and PDFs generated without the wire channel, added together in proportion to their respective contribution to the total live time of the Run 2a data set (i.e., $\mathrm{PDF_{mod}} = 0.948\ \mathrm{PDF_{def}} + 0.052\ \mathrm{PDF_{missing\ chan}}$). The shapes of these PDFs were compared using a Kolmogorov-Smirnov test, finding no significant difference. In addition, the efficiencies for the PDFs as calculated in simulation were compared and found to be consistent within $\sim$0.1%. The results of these studies imply that the resulting systematic error on the $2\nu\beta\beta$ measurement owing to this missing channel is less than 0.1%.

3. Energy scale for β-like events

As noted in Ref. [8], β-like energy depositions in the detector have a slightly different energy scale than γ-like deposits, and are reconstructed with $\sim$1% higher energy. The fit to the $2\nu\beta\beta$ spectrum yields a different estimate on this scale than from studies performed using the pair-production peak of ^{208}Tl. We choose to treat this difference as a systematic error, which contributes a 0.24% error to the $2\nu\beta\beta$ measurement.

TABLE VI. Summary of systematic errors determined via independent studies and explicitly included in the normalization term, N, in Eq. (13) (see Sec. IX B). The total, which is dominated by the systematic error from event selection cuts, is produced by adding in quadrature.

Component	Error (%)
Failed event reconstruction (Sec. IV D 2)	<0.18
Event selection (Sec. VIII)	2.53
Shape distortion (Sec. IX C 1)	0.33
Missing U-wire channel (Sec. IX C 2)	<0.1
β scale (Sec. IX C 3)	0.24
Background model (Sec. IX C 4)	0.25
Xe parameters (Sec. IX C 5)	0.26
Total	2.60

4. *Incomplete background model*

To test how an incomplete background model may affect the fit, two additional components (^{238}U and ^{232}Th chains in the HFE) were added to the model and the fit was rerun. These two components were chosen because they occupy the next largest amount of mass near the detector and the U and Th chains are generally likely sources of background. The results of this fit shifted the best-fit value of $2\nu\beta\beta$ counts <0.25%.

Additional possibilities were considered, including events arising from muons not vetoed by the muon veto. The total expected number of counts from such events with energy >700 keV over the Run 2a time period is $\lesssim$20, indicating a <0.1% effect when compared to the number of $2\nu\beta\beta$ counts.

The presence of the $2\nu\beta\beta$ decay of ^{134}Xe was also considered, but its low Q value (~820 keV) would mean only that the high-energy tail of the spectrum would contribute above the 700-keV analysis threshold. In addition, cross checks performed by increasing the analysis threshold and rerunning the fit found no evidence for additional background (see Fig. 29). Because of this, any contribution owing to ^{134}Xe was considered to be much less than 0.1%.

To accommodate the possibility of an incomplete background model, we include a systematic error of 0.25% on the $2\nu\beta\beta$ measurement.

5. *Xenon related*

The ^{136}Xe fraction in the ^{enr}Xe has been measured to be 80.672% ± 0.014% using dynamic dual-inlet mass spectroscopy [33], where the uncertainty is systematic. The abundance of ^{134}Xe is 19.098% ± 0.014% and other isotopes

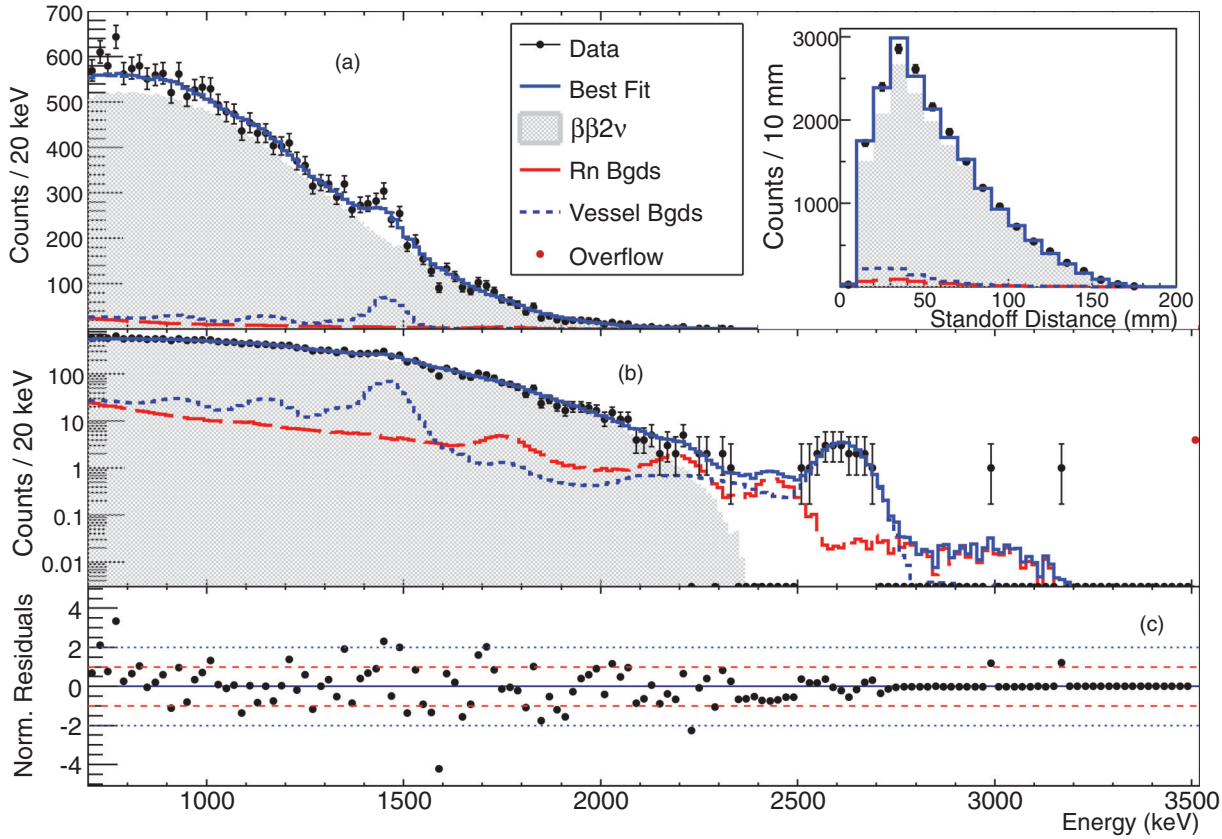

FIG. 26. (Color online) Fit results. Data and PDFs for SS energy spectra shown in linear (a), log (b), with residuals (c). The residuals have been normalized by the bin error. To improve visualization of the fit results, the energy bin widths in the plot are 20 keV instead of the 14-keV bin size used during fitting. SS standoff distribution is also shown (inset). Backgrounds have been grouped together according to Rn components and components in or near the TPC vessel. The best-fit counts and errors for each PDF are given in Table VII. There are fewer events in the $0\nu\beta\beta$ region of interest than in Ref. [8] because of the stricter fiducial volume cut.

make up for the remaining fraction of 0.230%, dominated by 0.203% of ^{132}Xe.

The isotope fraction is measured using a sample from the gas introduced into the detector at filling. The composition in liquid phase is expected to be the same as in the gas phase to <0.01% based on the difference of vapor pressures between ^{136}Xe and ^{130}Xe [34]. The conservative figure of 0.01% is used as a systematic error. In addition, some dilution of the ^{136}Xe content could have occurred because of the natural Xe used for detector commissioning desorbing over time from the plastic components inside the TPC. From solubility arguments this effect is estimated to be <0.04% and this figure is included as a systematic.

The temperature dependence of LXe density was measured by Refs. [35,36] and corrected to account for the small difference between ^{natl}Xe and ^{136}Xe. The stability of the temperature of the LXe was continuously monitored by thermocouples mounted on the cryostat during the course of data taking. A variation of 0.15 K rms was observed. The absolute temperature scale was calibrated in a test run before the start of the experiment with a reference RTD (then removed because of concerns about its radioactive background) yielding (166.6 ± 0.2) K, which translates to a density of 3.0305 ± 0.0077 g/cm^3. This absolute temperature is consistent with that obtained as a cross check by measuring the pressure at the onset of condensation when the detector was filled. The quadratic sum of the absolute temperature uncertainty (0.2 K) and the temperature swing observed by the thermocouples (0.15 K) results in a 0.06% uncertainty of the LXe density. The Xe-related systematics, listed above, contribute a $\pm$0.26% systematic error to the $2\nu\beta\beta$ measurement.

Table VI summarizes the numbers used as systematic error input to the final fit.

D. Fit results

To obtain the best-fit model, all parameters ($\boldsymbol{n}$, $\boldsymbol{s}$, and N) were allowed to float and $-\ln L$, defined by Eq. (13), was minimized. The errors on the main parameter of interest, $n_{2\nu\beta\beta}$, were determined by performing a profile likelihood scan. Figure 26 shows the results of this fit for SS events projected onto the energy axes. The projection onto the SD axis is provided in the inset. The corresponding spectra for MS events are shown in Fig. 27.

The best-fit value for $2\nu\beta\beta$ corresponds to 19 042 events above 700 keV. The total error on this value is estimated by performing a profile likelihood scan, yielding a 1σ error of 538 events, which incorporates the systematic errors from Table VI. The total exposure of ^{136}Xe is 23.14 kg yr and the overall detection efficiency (including the energy spectral cut) for $2\nu\beta\beta$ events is 57.88%. This with the molar mass of 135.514 g/mol translates into a $2\nu\beta\beta$ half-life of

$$T_{1/2}^{2\nu\beta\beta} = 2.165 \pm 0.016(\text{stat}) \pm 0.059(\text{sys}) \times 10^{21} \text{ yr}.$$

The best-fit values and associated errors for the counts of the component PDFs are listed in Table VII.[1] The breakdown

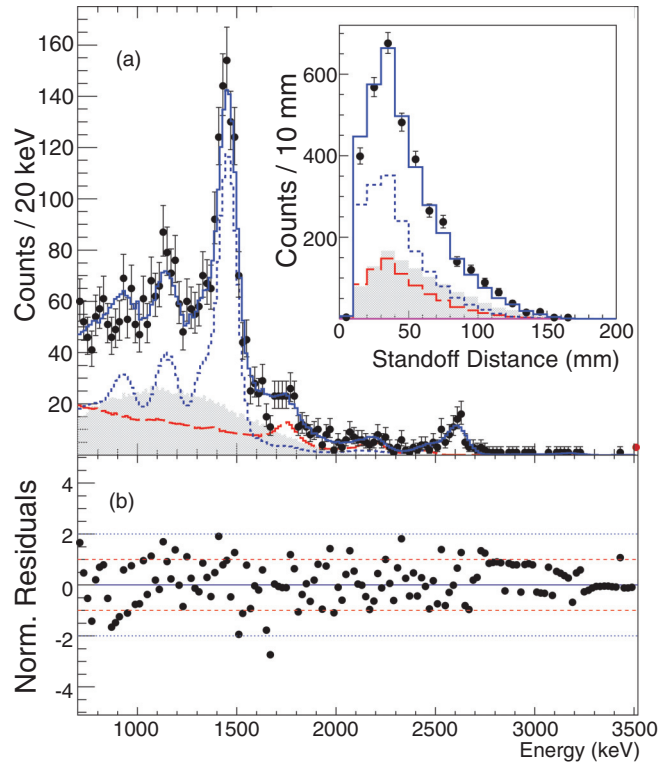

FIG. 27. (Color online) Projected MS energy spectra (a) and corresponding MS SD distribution (inset) for the final fit results. Residuals are shown in (b). PDF components are as in Fig. 26.

of the contributions from various error sources on the total error on the $2\nu\beta\beta$ measurement is given in Table VIII. Finally, this result is compared to other measurements of the $2\nu\beta\beta$ half-life of ^{136}Xe in Fig. 28.

The cumulative χ^2 for the projected energy and SD distributions shown in Figs. 26 and 27 are, respectively, 100.1 and 22.8 (94.0 and 23.2) for SS (MS) events. Because the best-fit parameters were determined using a ML fit, it is not possible to directly calculate the degrees of freedom (NDF) from the number of parameters and bins (see, e.g., Ref. [38]). Instead, the NDFs for each of the four projection distributions were estimated using toy Monte Carlo simulations, performed

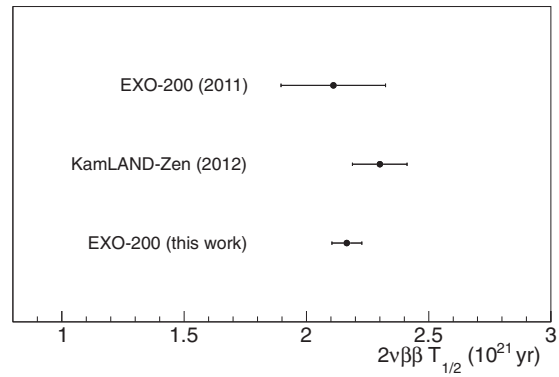

FIG. 28. A comparison of this result with EXO-200 (2011) [3] and KamLAND-Zen (2012) [37].

[1]We plan to present a full study of the background contributions in an upcoming publication.

TABLE VII. Summary of fit results for counts of the component PDFs in the fit model. Counts are the total integrated number above 700 keV across *both* the SS and the MS spectra. The errors quoted are estimated from MIGRAD and are not produced using profile-likelihood scans. ^{54}Mn in the Cu vessel, $0\nu\beta\beta$, and ^{135}Xe are omitted from this table because their best-fit values are consistent with 0. The division of background components is as given in Figs. 26 and 27.

PDF type		Counts
Cu vessel backgrounds		
	^{60}Co	560 ± 70
	^{40}K	1430 ± 70
	^{232}Th	590 ± 50
	^{238}U	90 ± 100
	^{65}Zn	110 ± 50
Rn backgrounds		
TPC cathode		
	^{214}Bi	18 ± 1
Active LXe		
	^{222}Rn	63 ± 4
Air gap		
	^{214}Bi	1100 ± 200
Inactive LXe		
	^{222}Rn	44 ± 3

by generating a toy data set from the best-fit parameters and rerunning the fit 5000 times. This study estimates the NDF for energy and standoff distributions to be, respectively, 113.7 and 17.2 (106.8 and 13.6) for SS and MS events, yielding a reduced χ^2 of 0.88 and 1.33 (0.88 and 1.70).

A typical quantity to compare results between experiments is the observed signal-to-background ratio (SBR). Because the ML fit is performed with two observables (energy and SD) and across two classes of events (SS and MS), it is difficult to define one number quantifying this ratio. However, the $2\nu\beta\beta$ signal

TABLE VIII. Summary of estimates of contributions to the final total error on $2\nu\beta\beta$ owing to various components. Note that this includes errors explicitly included in the normalization term (from Table VI) in addition to errors arising from other nuisance parameters (e.g., SS fraction). The total error is taken from the profile-likelihood scan (PLL) and is *not* a simple sum in quadrature as the components are correlated. To estimate the statistical error, all nuisance parameters except the $2\nu\beta\beta$ counts are fixed to their best-fit values and the PLL rerun. To estimate the error component owing to other sets of nuisance parameters, the following procedure is followed: After the best-fit parameters are found, the PLL is regenerated after fixing the relevant nuisance parameters to their best-fit values. The reduction of width in the resulting PLL from the original PLL yields the estimate on the error owing to the particular component(s).

Component	Error (%)
Systematic errors from Table VI	2.60
SS/(SS+MS) fraction	0.77
Backgrounds	1.3
Statistical	0.76
Total	2.83

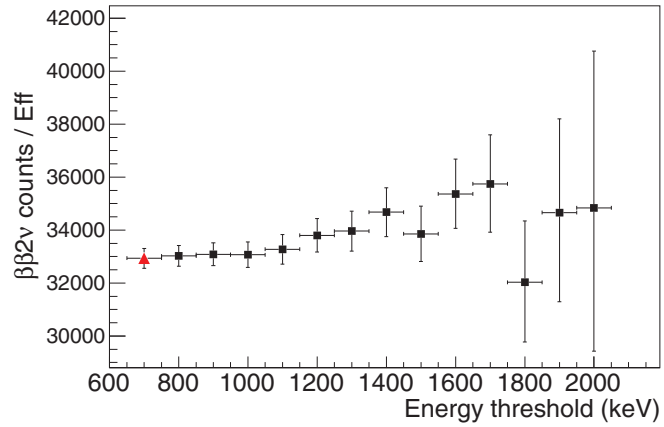

FIG. 29. (Color online) The fit count rate divided by efficiency of $2\nu\beta\beta$ versus energy threshold. The main result is the (red) triangle at 700 keV.

is observed to be 95% SS, consistent within the estimated systematic errors with the 98% SS predicted by the EXO-200 simulation, and so we may consider the SBR quantity purely in this class of events. The average SBR over the SS spectra is roughly 11. This quantity increases to 16 (19) as one selects the inner 60% (40%) of the fiducial volume, demonstrating the self-shielding of the xenon in addition to the power of fitting over the SD observable.

E. Final cross checks

A series of cross checks was performed on the fit result. The rate of $2\nu\beta\beta$ was binned versus time and the fit repeated for each time bin. The results were found to be consistent with a constant rate. In addition, an energy-only (without SD) fit was performed, producing a best-fit $2\nu\beta\beta$ count value 3.0% less than the reported result. The corresponding contribution from the backgrounds on the total error increased slightly from 1.3% (Table VIII) to 1.35% for the energy-only fit.

In addition to the studies performed in Sec. IX C 4, further investigations were undertaken to test the possibility that an unknown or unconsidered background is affecting the results of the fit. It is important to note that the measured goodness of fit is already an indication that the chosen fit model describes the data well. This suggests that, for an unknown background to affect the $2\nu\beta\beta$ measurement, it would need to exhibit an energy spectrum and SD distribution similar to $2\nu\beta\beta$ decay. As in Ref. [3] we consider two candidates satisfying these requirements, ^{90}Y and ^{188}Re, supported by ^{90}Sr and ^{188}W, which have half-lives of 28.90 yr and 69.78 d, respectively. It is important to note that the presence of these isotopes in the LXe is considered *a priori* unlikely as no indication of more common contaminants (e.g., metallic components from the U and Th chains) has been seen and the LXe is being continuously purified.

A ML fit to the Run 2a data set with an added time dimension was performed, including a PDF from ^{188}Re with an exponentially decaying time component corresponding to the ^{188}W half-life. The results of this fit found the number of counts of ^{188}Re to be consistent with zero and produced

a best-fit value of $2\nu\beta\beta$ within 0.8% of the quoted value. To investigate any effect owing to ^{90}Y, a ML fit was performed by adding a ^{90}Y PDF to the standard set of PDFs. The results of this fit produced a best-fit value of $2\nu\beta\beta$ within 3% of the quoted value.

A final cross check consisted of performing the fit with increasing energy thresholds. The purpose of this cross check is to investigate the possible presence of other unexpected backgrounds from β decays under the $2\nu\beta\beta$ spectrum. Increasing the energy threshold would change the relative contribution of any potential background, which would manifest as a change in the fit number of $2\nu\beta\beta$ events. The results of this study are shown in Fig. 29, demonstrating that the $2\nu\beta\beta$ measured rate is stable under even large changes of threshold.

X. CONCLUSIONS

We have reported on an improved measurement of the $2\nu\beta\beta$ decay of ^{136}Xe using 127.6 days of live time collected between September 2011 and April 2012. The resulting half-life $T_{1/2}^{2\nu\beta\beta} = 2.165 \pm 0.016(\text{stat}) \pm 0.059(\text{sys}) \times 10^{21}$ yr is measured with a total relative uncertainty of 2.83% and is dominated by systematic uncertainties. This half-life corresponds to a nuclear matrix element of $M^{2\nu} = 0.0218 \pm 0.0003$ MeV^{-1}, the smallest among the isotopes measured to date. For comparison, in Table IX we have tabulated the most precise half-life measurement of all nine nuclei for which $2\nu\beta\beta$ decay has been directly observed. The corresponding matrix elements $M^{2\nu}$ are included in this table as well. We note that ^{136}Xe has both the longest $2\nu\beta\beta$ half-life of any such decay and, as reported in this article, the most precise measurement.

We have described in some detail the data-analysis methods used for this measurement. These methods are similar to those employed to search for the $0\nu\beta\beta$ decay that, if observed, would indicate the discovery of new physics beyond the standard model. While the level of precision achieved here is not required for the $0\nu\beta\beta$ decay search, it demonstrates the quality of the EXO-200 data and the power of a fully active, high-resolution tracking detector with very low background.

Since April 2012 EXO-200 has accumulated an exposure several times larger than that described here. We expect to report the results of a new search for $0\nu\beta\beta$ based on this larger data set in the near future.

ACKNOWLEDGMENTS

EXO-200 is supported by the DOE and the NSF in the United States, the NSERC in Canada, the SNF in Switzerland, the NRF in Korea, the RFBR (12-02-12145) in Russia, and the DFG Cluster of Excellence "Universe" in Germany. EXO-200 data analysis and simulation uses resources of the National Energy Research Scientific Computing Center (NERSC), which is supported by the Office of Science of the U.S. Department of Energy under Contract No. DE-AC02-05CH11231. The collaboration gratefully acknowledges the WIPP for the hospitality and Dr. J. P. Severinghaus of the Scripps Institution of Oceanography for the accurate measurement of the isotopic composition of the EXO-200 enriched xenon.

APPENDIX: RECONSTRUCTION CLUSTERING DISTRIBUTION FUNCTIONS

Several PDFs are used when matching together U- and V-signal bundles and are described in the following.

1. Energy

The amplitude of the induced signals is directly proportional to the amplitude of the deposition signals, and so this correlation may be used when combining U and V signals. The energy PDF, estimated from fits to source data, quantifies

TABLE IX. Listing of the most precise measurements of $2\nu\beta\beta$ half-lives for each isotope as reported in the literature. Only direct counting experiments and ground-state decays are shown here. The results are listed chronologically by year of publication. Also included are phase-space factors ($G^{2\nu}$, from Ref. [5]) and nuclear matrix elements ($M^{2\nu}$) as defined by Eq. (1). The total relative uncertainty on the half-life is the quadratic sum of statistic and systematic errors, as given in the cited publications, divided by the half-life. The uncertainty in $M^{2\nu}$ is derived from the experimental uncertainty on $T_{1/2}^{2\nu}$, under the assumption that the uncertainties in $G^{2\nu}$ and g_A are negligible. In addition, these errors are determined to be symmetric or asymmetric following the same conventions used in assigning the half-life errors.

Nuclide	$T_{1/2}^{2\nu\beta\beta} \pm \text{stat} \pm \text{sys}$ (yr)	Relative uncertainty (%)	$G^{2\nu}$ (10^{-21} yr^{-1})	$M^{2\nu}$ (MeV^{-1})	Relative uncertainty (%)	Experiment (yr)
^{136}Xe	$2.165 \pm 0.016 \pm 0.059 \times 10^{21}$	± 2.83	1433	0.0218	± 1.4	EXO-200 (this work)
^{76}Ge	$1.84^{+0.09+0.11}_{-0.08-0.06} \times 10^{21}$	$^{+7.7}_{-5.4}$	48.17	0.129	$^{+3.9}_{-2.8}$	GERDA [39] (2013)
^{130}Te	$7.0 \pm 0.9 \pm 1.1 \times 10^{20}$	± 20.3	1529	0.0371	± 10.2	NEMO-3 [40] (2011)
^{116}Cd	$2.8 \pm 0.1 \pm 0.3 \times 10^{19}$	± 11.3	2764	0.138	± 5.7	NEMO-3 [41] (2010)
^{48}Ca	$4.4^{+0.5}_{-0.4} \pm 0.4 \times 10^{19}$	$^{+14.6}_{-12.9}$	15550	0.0464	$^{+7.3}_{-6.4}$	NEMO-3 [41] (2010)
^{96}Zr	$2.35 \pm 0.14 \pm 0.16 \times 10^{19}$	± 9.1	6816	0.0959	± 4.5	NEMO-3 [42] (2010)
^{150}Nd	$9.11^{+0.25}_{-0.22} \pm 0.63 \times 10^{18}$	$^{+7.4}_{-7.3}$	36430	0.0666	$^{+3.7}_{-3.7}$	NEMO-3 [43] (2009)
^{100}Mo	$7.11 \pm 0.02 \pm 0.54 \times 10^{18}$	± 7.6	3308	0.250	± 3.8	NEMO-3 [44] (2005)
^{82}Se	$9.6 \pm 0.3 \pm 1.0 \times 10^{19}$	± 10.9	1596	0.0980	± 5.4	NEMO-3 [44] (2005)

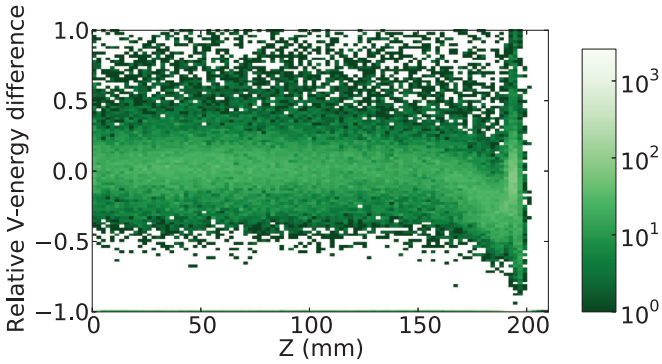

FIG. 30. (Color online) Total $[E_V - \rho_E(E_U)]/\rho_E(E_U)$ for an event, data from Th source runs as well as low-background runs. There is a strong Z dependence for $|Z| > 160$ mm observed, and so the energy relationship between U and V bundles is ignored for bundles in this region.

a relationship,

$$f_{\text{energy}}(E_U, E_V, Z) = \begin{cases} A & |Z| > 160 \text{ mm}, \\ A \exp\left[-0.5\left(\frac{\rho_E(E_U) - E_V}{\sigma_E(E_U)}\right)\right] & |Z| \leqslant 160 \text{ mm}, \end{cases} \quad \text{(A1)}$$

where A is a normalization constant, $E_{U,V}$ are the amplitudes of the U and V bundles, respectively, in units of gain-corrected ADC counts (i.e., ADC_U, ADC_V).[2] ρ_E is the expected value of E_V given a particular E_U and is defined as

$$\rho_E(E_U) = \begin{cases} 0 \text{ ADC}_V & E_U < -b_E/m_E, \\ E_U m_E + b_E & E_U \geqslant -b_E/m_E, \end{cases} \quad \text{(A2)}$$

with the constants b_E and m_E measured as -30.79 $\text{ADC}_V/\text{ADC}_U$ and 0.2378 ADC_V. σ_E from Eq. (A1) is the expected spread in E_V given a particular E_U and is defined as

$$\sigma_E(E_U) = \begin{cases} a_E & E_U < 350 \text{ ADC}_U, \\ c_E E_U + d_E \sqrt{E_U} & E_U \geqslant 350 \text{ ADC}_U, \end{cases} \quad \text{(A3)}$$

a_E, c_E, and d_E are constants with values of 20.22 ADC_V, 0.0101 $\text{ADC}_V/\text{ADC}_U$, and 0.892 $\text{ADC}_V/\text{ADC}_U{}^{1/2}$, respectively. All values of the constants quoted above are extracted from fits to calibration source data. Figure 30 shows a comparison using calibration data of the expected value of E_V [Eq. (A2)] with the true value of E_V.

At $|Z| > 160$ mm, effects from the anode begin to distort the reconstructed amplitudes of V wires. This comes from the fact that the V-wire shapes change somewhat when charge is deposited closer to the anode and the method for extracting the V-wire amplitudes (fitting with a signal model) uses a template from charge deposits in the bulk.

[2]The ADC_U unit value is very similar to keV; however, the data are not fully calibrated at this point of processing.

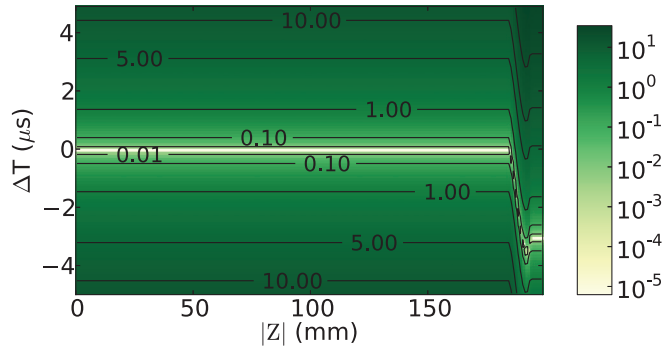

FIG. 31. (Color online) Visualization of time [Eq. (A4)] PDF used to cluster signal bundles together. The Z direction (color, contour lines) of the plot is the negative log of the indicated PDF: a lower value denotes a higher probability, with 0 (white) being the highest probable state.

2. Time

The relationship between the arrival times of U and V bundles has almost no dependence on the Z position of the bundles throughout most of the TPC, but yields a Z dependence as the bundles near the anode. This is a relic of reconstruction of V wires near the anode. The time PDF is a Gaussian with a Z-dependent mean,

$$f_{\text{time}}(t_U, t_V, Z) = B \exp\left\{-0.5\left[\frac{t_U - t_V - \rho_t(Z)}{\sigma_{\text{time}}}\right]^2\right\}, \quad \text{(A4)}$$

where B is a normalization constant, $t_{U,V}$ are the times in μs of the U and V bundles, respectively, σ_{time} is a constant (1 μs), and $\rho(Z)$ is given by

$$\rho_t(Z) = \begin{cases} 0\ \mu\text{s} & \frac{|Z|}{\text{mm}} \leqslant 185.2, \\ \rho_0 + \rho_1 Z' + \rho_2 Z'^2 - \rho_3 Z'^3 & 185.2 < \frac{|Z|}{\text{mm}} \leqslant 194.1, \\ 3\ \mu\text{s} & 194.1 < \frac{|Z|}{\text{mm}}, \end{cases} \quad \text{(A5)}$$

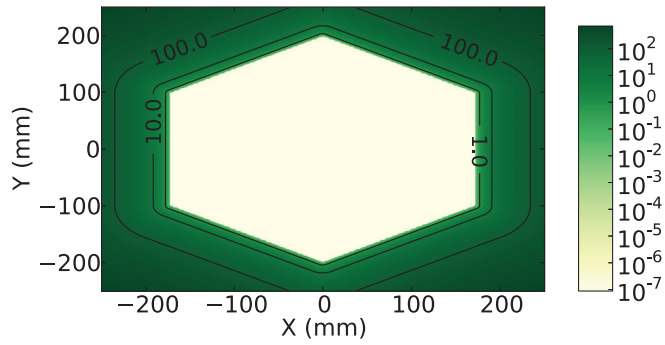

FIG. 32. (Color online) As in Fig. 31, but for the position PDF [Eq. (A6)].

where $Z' = |Z| - 190$ mm, to accommodate the symmetry of the two TPCs and ρ_0, ρ_1, ρ_2, and ρ_3 are 2.73 μs, 0.55 μs mm^{-1}, -0.065 μs mm^{-2}, and -0.013 μs mm^{-3}, respectively. A visualization of the time PDF is shown in Fig. 31.

3. *U*,*V* position

To ensure that only physically possible connections between U and V bundles are created, a regular hexagon is used as position PDF. The side-to-side diameter of the hexagon, defined by the detector geometry, is 342 mm. The PDF is given by

$$f_{UV\mathrm{pos}}(U,V) = \begin{cases} C & U,V \text{ inside hexagon,} \\ C\exp\left[-0.5\left(\frac{x_{\mathrm{perp}}}{\sigma_{UV}}\right)^2\right] & U,V \text{ outside hexagon,} \end{cases} \tag{A6}$$

where C is a normalization constant, x_{perp} is the nearest distance to a hexagon side, and $\sigma_{UV} = l/2 = 4.5$ mm, where l is the width of a single wire channel (9 mm). See Fig. 32 for a plot of the position PDF.

[1] J. Beringer, J. F. Arguin, R. M. Barnett, K. Copic *et al.* (Particle Data Group), Phys. Rev. D **86**, 010001 (2012).
[2] A. S. Barabash, Phys. Rev. C **81**, 035501 (2010).
[3] N. Ackerman *et al.* (EXO-200 Collaboration), Phys. Rev. Lett. **107**, 212501 (2011).
[4] A. Gando *et al.* (KamLAND-Zen Collaboration), Phys. Rev. C **85**, 045504 (2012).
[5] J. Kotila and F. Iachello, Phys. Rev. C **85**, 034316 (2012).
[6] P. Vogel, J. Phys. G: Nucl. Part. Phys. **39**, 124002 (2012).
[7] V. Rodin, A. Faessler, F. Simkovic, and P. Vogel, Nucl. Phys. A **766**, 107 (2006).
[8] M. Auger *et al.* (EXO-200 Collaboration), Phys. Rev. Lett. **109**, 032505 (2012).
[9] H. Klapdor-Kleingrothaus and I. Krivosheina, Mod. Phys. Lett. A **21**, 1547 (2006).
[10] A. Gando *et al.* (KamLAND-Zen Collaboration), Phys. Rev. Lett. **110**, 062502 (2013).
[11] M. Auger *et al.*, J. Instrum. **7**, P05010 (2012).
[12] R. Neilson, F. LePort, A. Pocar, K. Kumar, A. Odian *et al.*, Nucl. Instrum. Methods Phys. Res., Sect. A **608**, 68 (2009).
[13] L. S. Miller, S. Howe, and W. E. Spear, Phys. Rev. **166**, 871 (1968).
[14] F. LePort, R. Neilson, P. Barbeau, K. Barry, L. Bartoszek *et al.*, Rev. Sci. Instrum. **82**, 105114 (2011).
[15] 3M HFE-7000, http://www.3m.com
[16] H. Gemmeke, G. Drexlin, V. Eberhard, G. Giorginis, W. Grandegger *et al.*, Nucl. Instrum. Methods Phys. Res., Sect. A **289**, 490 (1990).
[17] E.-I. Esch, T. Bowles, A. Hime, A. Pichlmaier, R. Reifarth *et al.*, Nucl. Instrum. Methods Phys. Res., Sect. A **538**, 516 (2005).
[18] D. Leonard, P. Grinberg, P. Weber, E. Baussan, Z. Djurcic *et al.*, Nucl. Instrum. Methods Phys. Res., Sect. A **591**, 490 (2008).
[19] A. Dobi, C. Hall, S. Slutsky, Y. Yen, B. Aharmin *et al.*, Nucl. Instrum. Methods Phys. Res., Sect. A **675**, 40 (2012).
[20] R. Brun and F. Rademakers, Nucl. Instrum. Methods Phys. Res., Sect. A **389**, 81 (1997).
[21] E. Conti, R. DeVoe, G. Gratta, T. Koffas, S. Waldman *et al.*, Phys. Rev. B **68**, 054201 (2003).
[22] J. Allison, K. Amako, J. Apostolakis *et al.*, IEEE Trans. Nucl. Sci. **53**, 270 (2006).
[23] ANSYS, Maxwell 2D, http://www.ansys.com
[24] S. Ramo, Proc. IRE **27**, 584 (1939); W. Shockley, J. Appl. Phys. **9**, 635 (1938).
[25] T. Doke, Nucl. Instrum. Methods Phys. Res. **196**, 87 (1982).
[26] Sealing Technol. **2010**, 4 (2010), COMSOL, http://www.comsol.com
[27] D. North, Proc. IEEE **51**, 1016 (1963).
[28] V. T. Jordanov and G. F. Knoll, Nucl. Instrum. Methods Phys. Res., Sect. A **345**, 337 (1994).
[29] F. James and M. Roos, Comput. Phys. Commun. **10**, 343 (1975).
[30] A. Göök, F.-J. Hambsch, A. Oberstedt, and S. Oberstedt, Nucl. Instrum. Methods Phys. Res., Sect. A **664**, 289 (2012).
[31] R. Patterson, Ph.D. thesis, Princeton University, 2007.
[32] G. Schenter and P. Vogel, Nucl. Sci. Eng. **83**, 393 (1983).
[33] J. Severinghaus (private communication).
[34] G. Jancso and W. A. Van Hook, Chem. Rev. **74**, 689 (1974).
[35] M. Terry, J. Lynch, M. Bunclark, K. Mansell, and L. Staveley, J. Chem. Thermodyn. **1**, 413 (1969).
[36] V. A. Rabinovich and L. S. Veklser, in *Thermophysical Properties of Matter and Substances*, edited by V. A. Rabinovich, Vol. 2 (Amerind Publishing, New Delhi for U.S. National Bureau of Standards, 1974); data reproduced in N. B. Vargaftik, *Tables on the Thermophysical Properties of Liquids and Gases*, 2nd ed. (Wiley & Sons, New York, 1975).
[37] A. Gando *et al.* (KamLAND-Zen Collaboration), Phys. Rev. C **86**, 021601 (2012).
[38] H. Chernoff and E. Lehmann, Ann. Math. Stat. **25**, 579 (1954).
[39] M. Agostini *et al.* (GERDA Collaboration), J. Phys. G: Nucl. Part. Phys. **40**, 035110 (2013).
[40] R. Arnold *et al.* (NEMO-3 Collaboration), Phys. Rev. Lett. **107**, 062504 (2011).
[41] A. Barabash and V. Brudanin (NEMO Collaboration), Phys. Atom. Nucl. **74**, 312 (2011).
[42] J. Argyriades *et al.* (NEMO-3 Collaboration), Nucl. Phys. A **847**, 168 (2010).
[43] J. Argyriades *et al.* (NEMO Collaboration), Phys. Rev. C **80**, 032501 (2009).
[44] R. Arnold *et al.* (NEMO Collaboration), Phys. Rev. Lett. **95**, 182302 (2005).